Materials Science & Engineering A 975 (2026) 150913

Contents lists available at ScienceDirect

Materials Science & Engineering A

journal homepage: www.elsevier.com/locate/msea

Overload-induced fatigue crack growth retardation in LPBF Inconel 718: role of anisotropic microstructure and crack closure mechanisms

J.A. Aguilera [a], P.M. Cerezo [a], A.S. Cruces [a], T. Guraya [b], F. Paysan [c], J. Gussone [c], E. Breitbarth [c], P. Lopez-Crespo [a,*]

[a] Department of Civil and Materials Engineering, University of Malaga, C/Dr Ortiz Ramos S/n, Malaga, 29071, Spain
[b] Faculty of Engineering of Bilbao, University of the Basque Country (UPV/EHU), Bilbao, E48013, Spain
[c] German Aerospace Center (DLR), Institute for Frontier Materials on Earth and in Space, Linder Hoehe, Cologne, 51147, Germany

ARTICLE INFO

Keywords:
Additive manufacturing
Alloy 718
Crack closure
Fatigue crack growth
Overload

ABSTRACT

Additive manufacturing (AM) via laser powder bed fusion (LPBF) induces a severe crystallographic anisotropy to Inconel 718 (IN718). Its influence on fatigue crack growth under variable amplitude loading requires high-resolution micromechanical analysis. This study provides a mechanistic evaluation of overload-induced crack growth retardation in as-built LPBF IN718 across two build orientations (0° and 90°), compared against a wrought baseline. Employing a single-specimen, continuum-to-microstructural scale methodology to deeply profile localised interactions, crack growth was tracked under constant load amplitude interrupted by a single tensile overload. In-situ digital image correlation quantified local crack opening behaviours, coupled with EBSD, XRD, and fractography to characterise active microstructural deformation and residual stress states. While the wrought condition exhibited lower nominal crack growth rates than the LPBF ones, normalising the driving force to the effective stress intensity factor (ΔK_{eff}) caused all responses to converge in the stable Paris regime, indicating comparable intrinsic propagation resistance. Following the overload, AM builds exhibited a severely truncated retardation zone compared to the wrought alloy. Fractography revealed that AM closure is driven by a combination of roughness-induced—characterised by tortuous deflections against columnar grains—and plasticity-induced crack closure. Crucially, despite diverging macroscopic yield strengths between AM orientations, their retardation spatial extents were identical. This implies a disconnect in LPBF IN718: the localised transient retardation behaviour does not simply follow the plastic zone dimensions predicted by the bulk macroscopic yield strength.

NOMENCLATURE

Symbol/Abbreviation	Description
2θ	Scattering angle
a	Crack length
AM	Additive manufacturing
B	Specimen thickness
BD	Building direction
C(T)	Compact Tension specimen
CD	Crack direction
COD	Crack opening displacement
da/dN	Crack growth rate
ΔK_{NOM}	Nominal stress intensity factor range
ΔK_{eff}	Effective stress intensity factor range
ΔK_{th}	Sif threshold
ΔK	Stress intensity factor range
DIC	Digital image correlation
E	Macroscopic Young's modulus
EBSD	Electron backscatter diffraction
EDM	Electro discharge machining
FCG	Fatigue crack growth
FCGR	Fatigue crack growth rate
IPF	Inverse pole figures
K_I	Mode I stress intensity factor
K_{max}	Maximum stress intensity factor (load condition)
K_{op}	Opening SIF
LEFM	Linear elastic fracture mechanics
LPBF	Laser powder bed fusion

(continued on next column)

(continued)

(continued on next page)

* Corresponding author.
E-mail address: plopezcrespo@uma.es (P. Lopez-Crespo).

https://doi.org/10.1016/j.msea.2026.150913
Received 29 April 2026; Received in revised form 23 July 2026; Accepted 6 August 2026
Available online 7 August 2026
0921-5093/© 2026 The Authors. Published by Elsevier B.V. This is an open access article under the CC BY-NC-ND license (http://creativecommons.org/licenses/by-nc-nd/4.0/).

(*continued*)

Symbol/Abbreviation	Description
N	Number of cycles
ν	Poisson's ratio
OL	Overload
PICC	Plasticity-induced crack closure
PZ	Plastic zone
R	Load ratio
r_p	Irwin's monotonic plastic zone
RICC	Roughness-induced crack closure
SIF	Stress intensity factor
σ_{YS}	Yield stress in uniaxial tension
σ_{yy}	Stress in the crack opening direction
W	Specimen width
XRD	X-ray Diffraction

1. Introduction

Nickel-based superalloys, particularly IN718, are widely used in high-temperature turbine applications owing to their exceptional mechanical properties [1,2]. In service, critical rotating components, such as turbine blades, are subjected to a spectrum of different loading conditions, including overloads (OL), rather than solely experiencing constant amplitude loading [3,4]. In conventionally wrought materials, the influence of tensile overloads has been extensively studied, revealing that such loads can significantly retard fatigue crack growth. This retardation is primarily attributable to crack shielding, which arises from both plasticity-induced crack closure (PICC) along the crack flanks and the compressive residual stresses developed within the enlarged plastic zone ahead of the crack tip [3,5–7]. In contrast, research on Additive Manufactured (AM) IN718, particularly Laser Powder Bed Fusion (LPBF), has predominantly focused on constant-amplitude cyclic loading, with emphasis on process parameters, defects, and the characterisation of fatigue crack propagation and threshold rates [1,8,9]. However, the interaction between single OL events and the anisotropic microstructure inherent to AM components remains insufficiently understood. In particular, it is unclear whether the retardation mechanisms established for isotropic wrought materials [4,10] remain valid in the presence of strong microstructural anisotropy. Understanding the influence of build orientation on post-overload fatigue behaviour is therefore essential for assessing the structural integrity of AM components in aerospace applications [4,11].

Fatigue crack propagation is conventionally described within the framework of Linear Elastic Fracture Mechanics (LEFM), where the crack growth rate (da/dN) is related to the applied stress intensity factor (SIF) range (ΔK) through the Paris–Erdogan law [11,12]. However, the intrinsic resistance to crack propagation is more accurately represented by the effective SIF range (ΔK_{eff}), which accounts for crack tip shielding mechanisms such as PICC or roughness-induced crack closure (RICC) [13,14]. Reported crack growth behaviour of LPBF and wrought IN718 is often comparable within the Paris regime, where continuum-scale deformation dominates [9,11]. Nevertheless, significant differences arise in the near-threshold regime, where crack propagation becomes sensitive to microstructural features. AM material typically exhibits lower threshold values and higher crack growth rates compared to wrought counterparts [1,9]. These differences originate from the distinct microstructures of the two materials. Wrought IN718 generally exhibits a homogeneous equiaxed grain structure, resulting in isotropic mechanical behaviour [1,15]. In contrast, LPBF produces a highly anisotropic microstructure characterised by columnar grains and strong ⟨001⟩ crystallographic texture, leading to orientation-dependent crack propagation behaviour [1,9,16]. In addition, process-induced defects and residual stresses further modify the effective crack driving force [13,17]. Tensile residual stresses can reduce crack closure and increase ΔK_{eff}, thereby accelerating crack growth, whereas compressive residual stresses promote closure and reduce the effective driving force [9,18]. Furthermore, crack path morphology is influenced by crystallographic features, resulting in tortuous paths in wrought material and a propagation behaviour that is dependent on the build direction in additively manufactured material [19,20].

A key limitation in conventional Fatigue Crack Growth (FCG) studies is the reliance on global measurement techniques, which are unable to resolve local variations in crack closure behaviour [21–23]. Digital Image Correlation (DIC) provides a powerful tool by enabling full-field displacement measurements with high spatial resolution, offering direct insights into local crack tip mechanics [4,24–26]. By extracting local Crack Opening Displacement (COD) profiles, it is possible to determine the opening stress intensity factor (K_{op}) and quantify the extent of crack closure [27,28]. This approach enables the evaluation of ΔK_{eff} to be evaluated based on local measurements [29], thereby enabling a more rigorous separation between intrinsic crack growth resistance and extrinsic shielding mechanisms. Such capability is particularly relevant for AM materials, where anisotropic microstructures lead to spatially heterogeneous deformation and crack closure behaviour [30–32].

This spatially heterogeneous crack closure becomes particularly critical when evaluating the transient effects of a tensile OL. An OL significantly amplifies localised shielding, introducing a complex transient effect in FCG: an immediate, brief acceleration in crack growth rate, followed by a delayed drop to a minimum and gradual recovery. Mechanistically, this retardation is driven by the formation of an enlarged plastic zone (r_p), which generates strong compressive residual stresses in closed cracks and promotes PICC [10,13,33,34]. While these PICC-driven mechanisms are well established for conventional wrought materials [3,4,7,10,14,33–37], their applicability to AM microstructures remains unclear. In LPBF IN718, the presence of columnar grains and strong crystallographic texture introduces strong anisotropy, which can significantly alter both the shape and the geometric constraint of the plastic zone. As a result, the development of crack closure and the extent of overload-induced retardation, due to its dependence on local yielding behaviour, are expected to depend on the build orientation [9,19,38].

The present study investigates overload-induced fatigue crack growth retardation in as-built LPBF IN718 for two build orientations (0° and 90°), in comparison with a wrought counterpart. The materials are analysed in the as-received condition to preserve their initial microstructural and residual stress states, thoughtfully isolating the fundamental influence of the as-built LPBF architecture without the confounding effects of thermal post-processing. By combining DIC, near-surface X-ray diffraction (XRD) residual stress measurements, and scanning electron microscopy fractographic analysis, the study establishes a direct relationship between microstructure, crack closure behaviour, and overload-induced retardation. It is hypothesised that overload-induced retardation in LPBF IN718 is reduced relative to the wrought condition due to constraints on plastic zone development imposed by microstructural anisotropy, and that build orientation primarily influences crack path morphology without significantly altering the magnitude of retardation. To the authors' knowledge, no previous study has directly quantified local crack closure evolution during overload-induced fatigue crack growth in LPBF IN718 using full-field DIC, enabling a direct comparison between AM and conventional microstructures.

Table 1
Powder IN718 composition.

Element	Ni	Cr	Fe	Nb + Ta	Mo	Ti	Al	C	Co	O
Composition (wt.%)	52.96	19.3	18.24	4.93	3	0.96	0.49	0.03	0.04	0.02

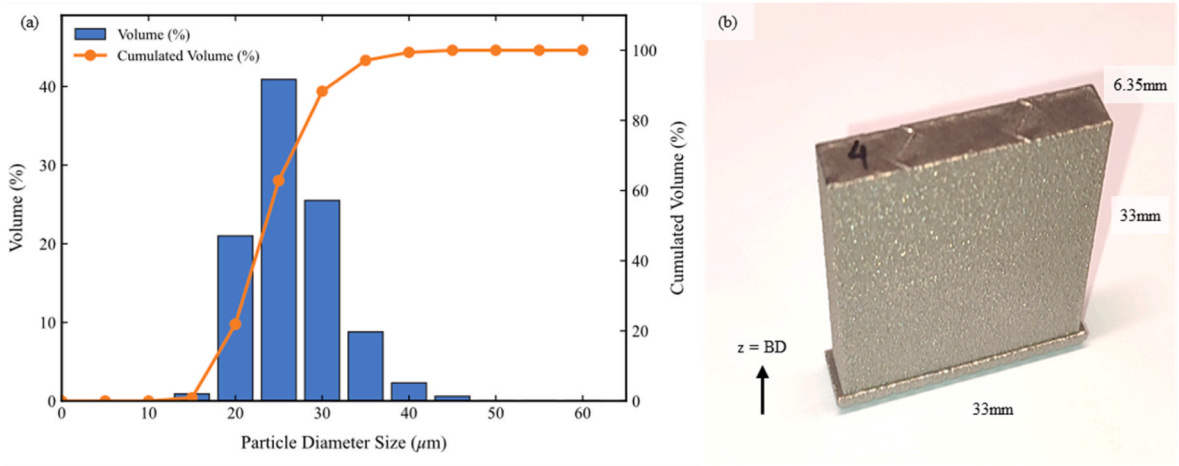


Fig. 1. (a) IN718 powder dimensions distribution. (b) Near net-shape AM block.

Table 2
Wrought IN718 composition.

Element	Ni	Cr	Fe	Nb + Ta	Mo	Ti	Al	C	Mn	Si	Cu	P	S	B
Composition (wt.%)	54.1	18.5	17.70 (balance)	4.955	3.04	0.94	0.52	0.012	0.04	0.09	0.03	0.007	<0.001	0.0040

2. Materials and methods

2.1. Material and additive manufacturing process

IN718 powder (Carpenter Additive) produced by gas atomisation was used as feedstock material for LPBF manufacturing. Chemical composition and powder distribution can be seen in Table 1 and Fig. 1 (a), respectively. Blocks of 33 mm × 33 mm were fabricated with a size near-net shape, Fig. 1(b), through LPBF using Renishaw AM500 (Bilbao, Spain). The IN718 used in this study was built with the following parameters P = 275 W, Hatch = 90 μm, a scan velocity of 1000 mm/s and a thickness of 60 μm per layer. The scan strategy used is a 67° rotation each layer. The mentioned parameters result in a nominal volumetric energy density of 51 Jmm^{-3}. A mean density of 8.16 g/cm^3 from 6 measurements following ASTM B311 [39] has been obtained, yielding a relative density of 99.6% compared to theoretical density of 8.19 gr/cm^3 [40]. No post-build heat treatment was applied in order to preserve the as-built microstructure and residual stress state, which are critical for assessing intrinsic anisotropy and its effect on fatigue behaviour. According to printer manufacturer [41], yield strength for 0° is 735 MPa and for 90° is 632 MPa in the as-built state, similar to those reported in literature for the as-built state [42–47]. Preliminary microstructure evaluation showed no difference between directions within the build plane, so the material is considered transversely isotropic.

The wrought reference alloy is VDM® Alloy 718 CTP (NICROFER 5219 CTP, material designation 2.4668, UNS N07718), manufactured by VDM Metals GmbH, with composition conformed to API 6ACRA specifications as shown in Table 2, with a measured density of 8.24 g/cm^3. According to the provider, room temperature mechanical properties were evaluated using longitudinal orientation specimens and according to ASTM E8/E8M [48], yielding a 0.2% offset yield strength of 877 MPa and ultimate tensile strength of 1219 MPa. The samples' hardness, after Vickers test with a 0.5 kgf load, were 374 HV for the wrought material and 304 HV for the AM samples.

Following ASTM E647 [49] standard a total of three Compact tension C(T) samples with W = 25 mm and B = 6 mm are manufactured, following the minimum width recommended by the standard and the required thickness relative to its width. C(T) with similar dimensions have been also employed in recent FCG tests for AM samples [9,50–52]. Two samples are machined from the LPBF blocks, Fig. 1(b), and one more from the Wrought alloy. For the three samples, same cutting process is followed; C(T) profiles are machined with wire cut electro discharge machining (EDM) and surfaces are milled at low speed till the final thickness. The AM blocks are machined with the notch manufactured parallel to the build direction in one sample and perpendicular to it in the other sample, resulting in a 0° or parallel CD//BD sample and a 90° or perpendicular CD⊥BD. The wrought sample (W) is machined in C-R direction according to ASTM E399 [53]. Given the resource-intensive nature of the *in-situ* DIC crack tracking coupled with continuum-to-microstructural scale characterisation (encompassing EBSD, XRD, and high-resolution fractography), a single specimen per condition was evaluated. This methodology prioritises the depth of mechanistic data over statistical bulk qualification and is a well-established practice in recent literature investigating localised fatigue phenomena in AM metals or other advanced materials [13,52,54–57]. Within each specimen, however, a high density of measurements was extracted continuously throughout the test, yielding thousands of instantaneous crack growth (da/dN) and closure data points that establish clear kinetic trends, alongside statistically robust averages for the nanoindentation and porosity analyses. While batch-level repeatability is not assessed, this intra-specimen data density supports confidence in the local trends reported. Consequently, this study is best understood as a high-resolution, mechanistic exploration of local crack closure phenomena and microstructural interactions, rather than a statistical bulk qualification of the materials tested.

2.2. Fatigue crack growth testing and digital image correlation

In order to analyse the fatigue behaviour of the material with a single OL, a constant load approach is taken according to ASTM E647 [49] including an OL in the three samples at approximately the same position, at a = 9.3 mm. Pre-cracking to a length of 6.5 mm was performed under constant amplitude loading at 10 Hz, with a stress ratio of R = 0.1 and a maximum load of 3 kN. The cyclic load is, as well, maintained constant throughout the experiment between 0.3 kN and 3 kN with a load ratio R = 0.1. The OL load is 4.5 kN, resulting in a $R_{OL} = 1.5$. A constant load amplitude approach was adopted to preserve the natural evolution of crack closure and residual stress effects during propagation. The fatigue crack initiation and propagation tests were performed using the Walter + Bai LFM-C 5 kN (Málaga, Spain) in-situ fatigue test machine. The

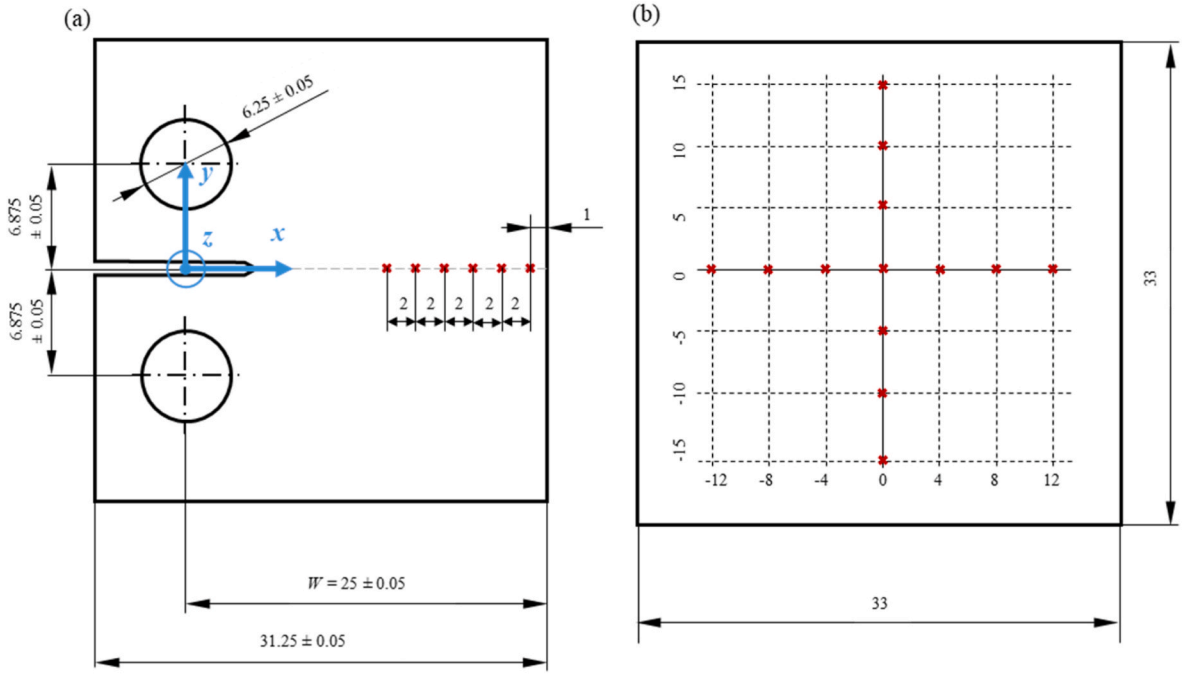


Fig. 2. (a) C(T) sample with XRD measured points (red crosses). (b) AM non cracked block with XRD measurement points (red crosses). (For interpretation of the references to colour in this figure legend, the reader is referred to the Web version of this article.)

fatigue cracking was done at a frequency of 10 Hz, but the loading rate was reduced to 0.1 Hz at various crack lengths to enable the acquisition of images of the fatigue cracking while loading and unloading.

On one side of the sample, images are taken in several crack lengths during maximum load, at intervals between 1000 and 2000 cycles before the OL and between 50 and 500 cycles after the OL. Crack length measurements were obtained by visual crack-tip location of the taken images, with an estimated measurement uncertainty of ±5 μm. The stereo microscope, a Questar QM-100 long-distance microscope, provides a field of view of approximately 2.5 × 2.5 mm, which then resulted in the need to translate the microscope to keep the crack in frame. The spatial resolution of the optics corresponds to approximately 1.2 μm/pixel. Due to the high magnification required for the small field of view, a scratching technique was used to generate an appropriately speckle pattern [58,59]. DIC analysis was conducted using a 59× 59 pixel subset and 3-pixel step size, due to its high inherent noise. Given the optical magnification, this setup provides an effective spatial resolution of 70.8 μm with a displacement data spacing of 3.6 μm. Crack tip and path coordinates were autonomously tracked using the CrackPy Python library [60–62], allowing extraction of COD data from a 100× 100 μm area located 75 μm behind the advancing crack-tip in horizontal direction and at 150 μm above and below the crack path, following similar steps to Paysan et al. [28]. This location was selected to ensure enough resolution for crack closure analysis. The COD data is later analysed based on the compliance method proposed by Moreno et al. [63] to obtain the normalised opening load (K_{op}/K_{max}). In this approach, the open-crack compliance is first established from the linear upper portion of the unloading branch, and the K_{op} is identified where the compliance of the loading branch deviates by a specific threshold. While a 2% offset is standard for wrought materials, a 4% threshold was utilised here. The tortuous crack paths in AM materials promote pronounced RICC and gradual asperity separation; thus, the 4% threshold prevents premature triggering from experimental noise or partial asperity contact, providing a more stable identification of when the entire crack is open, with the compromise of slightly overestimating the actual opening load.

2.3. Residual stress measurements protocol

Residual stress analysis was performed using XRD with the $\sin^2\psi$ method on the high-angle (331) and (420) reflections to minimise systematic errors. Measurements were conducted on a Bruker D8 Discover, Cu Kα radiation, (Cologne, Germany) and stress evaluation was conducted using Leptos 7 software (Bruker).

Residual stress measurements were performed on compact tension C(T) specimens following Fatigue crack growth rate (FCGR) testing, with no external load applied during XRD acquisition. No surface preparation was applied prior to initial measurements; samples were analysed in the as-tested condition to preserve the deformation-induced stress state. For cracked specimens, a total of six points were measured along the prospective ligament crack plane, starting at a distance of 1 mm from the specimen edge and progressing toward the final crack tip position with a spacing of 2 mm between consecutive points, Fig. 2(a). For AM uncracked reference specimens, measurements were obtained at multiple locations to characterise the initial residual stress distribution in the two directions, Fig. 2(b). The objective was to characterise the residual stress state resulting from the AM process, and to evaluate how these stresses redistribute and evolve after cyclic loading and crack propagation. Measured points consist of four 1 × 1 mm spots that are irradiated with exposure times of 150 s per frame to achieve adequate signal-to-noise ratios despite the elevated background caused by fluorescence effects. It should be noted that the results represent near-surface stress states (<10 μm depth).

2.4. Microstructural characterisation techniques

Samples were initially extracted from the compact tension specimens using an Accutom-5 precision cut-off machine (Struers). To accommodate the different analysis requirements, the characterisation was divided into three specific techniques:

- Fractography and Microstructural Analysis (SEM and Optical Microscope): Following the fatigue tests, the cracked region of each sample was extracted and sliced longitudinally through the mid-

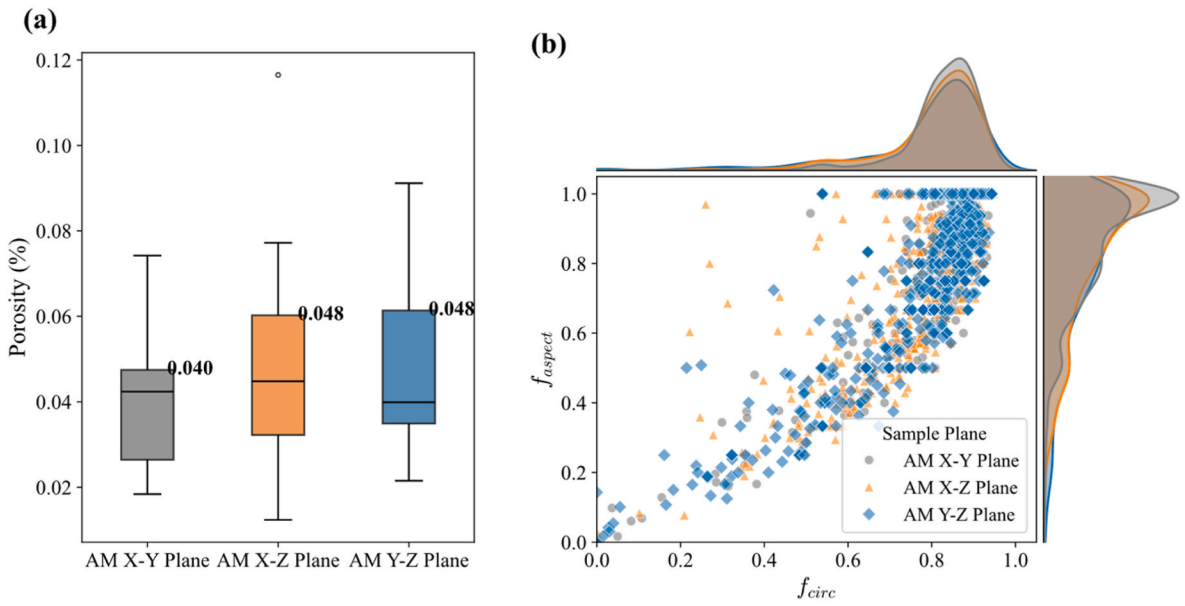


Fig. 3. Study of porosity via 2D metallography. (a) Porosity percentage for AM IN718 (X-Y, Y-Z, and X-Z planes). (b) Pore aspect ratio versus circularity, with marginal density plots, for each plane.

thickness. The resulting back half of this division was used for fractography. These samples were hot-mounted in carbon-filled conductive phenolic resin, subjected to standard grinding and polishing, and chemically etched using waterless Kaling's reagent No. 2 [64] to reveal microstructural features. Imaging was conducted using a scanning electron microscope (SEM, CLARA-TESCAN, Malaga, Spain). Three additional specimens (XY, XZ and YZ plane) were ground and polished to enable inspection of porosity by 2D metallography (optical microscope, LEICA DM6, Malaga, Spain). For each sample, an area of approximately 20 mm^2 was covered, providing a representative assessment of the internal porosity. Porosity was defined as the ratio of the total pore area to the image area. Circularity factor, $f_{circ} = \frac{4\pi A}{P^2}$, and aspect ratio, $f_{aspect} = \frac{\min(W,H)}{\max(W,H)}$, are also calculated, being P the pore perimeter, W the width and H the height of the pore.

- Crystallographic Analysis (EBSD): The front half of the longitudinally sectioned crack (which retained the surface used for DIC) was hot-

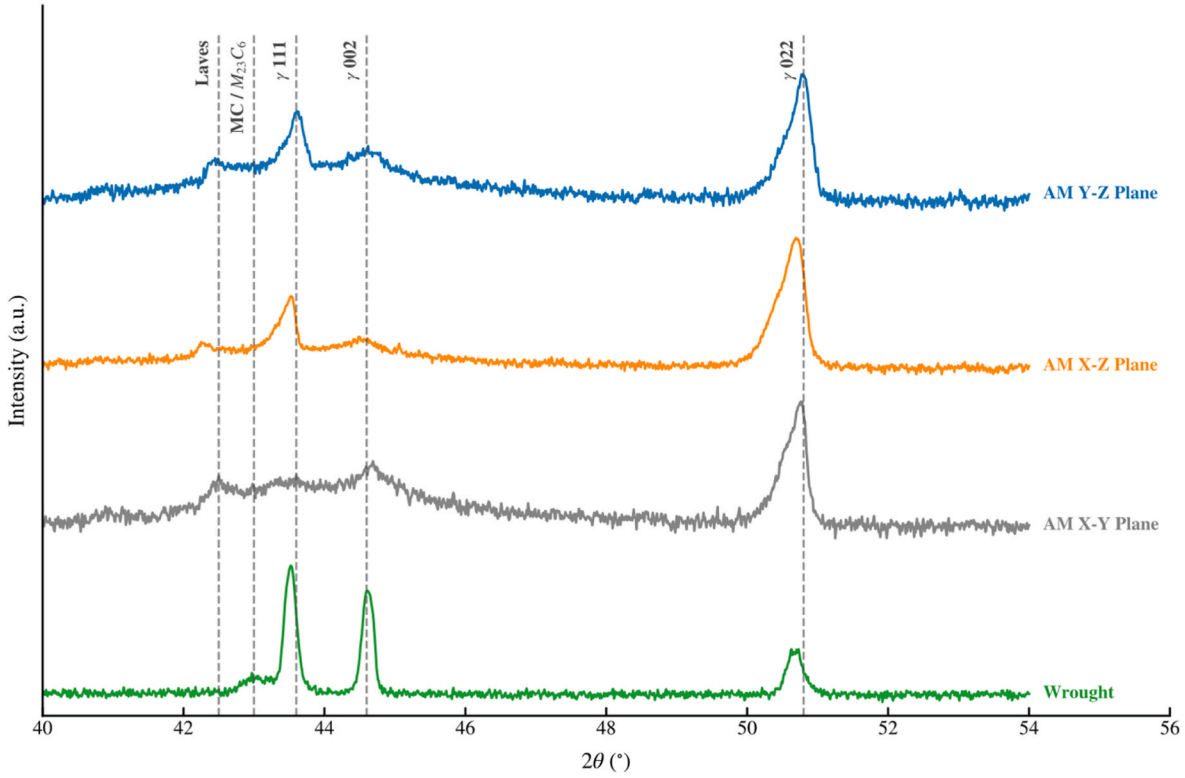


Fig. 4. XRD patterns ($2\theta = 40^\circ - 54^\circ$) of Wrought and AM IN718 (X-Y, Y-Z, and extracted X-Z planes). Data is stacked and normalised on a logarithmic scale. Vertical lines indicate theoretical peak locations.

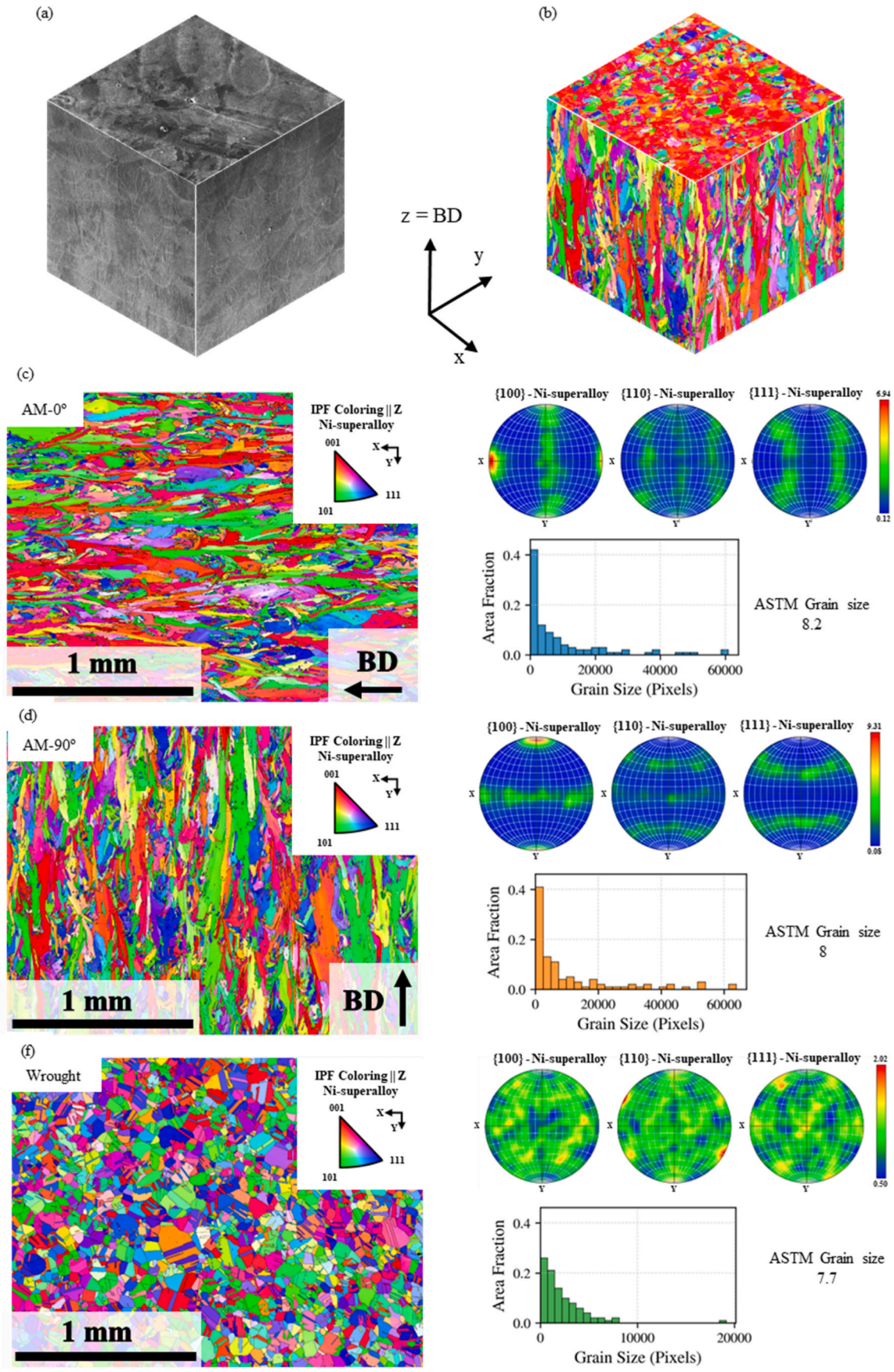


Fig. 5. (a) SEM micrographs of etched AM IN718, (b) 3D EBSD reconstruction, (c), (d) and (f) EBSD analysis for AM-0°, AM-90° and Wrought samples respectively, showing IPF colouring, pole figures, grain size distribution and ASTM grain size.

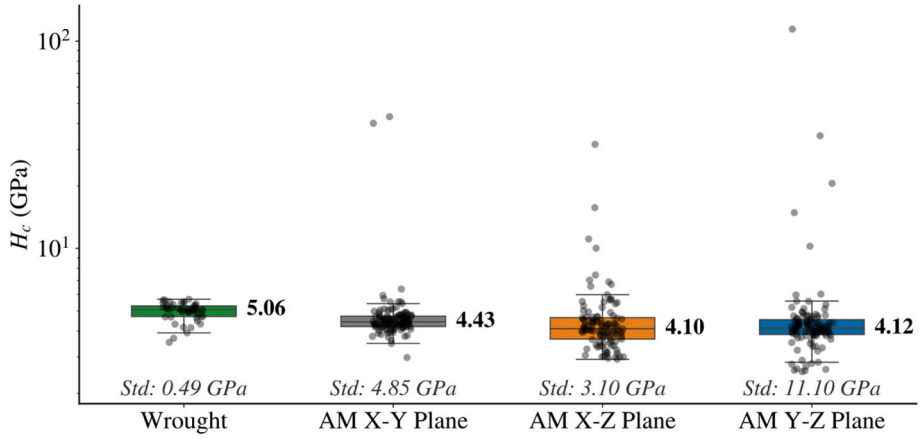


Fig. 6. Nanoindentation contact hardness (H_c) variability of Wrought and AM IN718 (X-Y, X-Z, and Y-Z planes).

mounted to keep the crack surface visible. In addition to standard polishing, an extra vibrational polishing step was conducted using an OP-U suspension with H_2O_2 on a Buehler VibroMet 2 for approximately 6 h to achieve a strain-free surface. EBSD was performed using a Zeiss Ultra 55 (Cologne, Germany) equipped with an Oxford Nordlys II detector. Large-area scans (2200 × 1700 μm) with a 1 μm step size were performed at the sample centre near the crack to capture the overall microstructural context, including grain morphology, texture, and crack propagation trajectory. In addition to them, AM-0° and AM-90° samples underwent to a higher resolution EBSD mapping with an area of 50 × 50 μm and a resolution of 0.1 μm step size in a location near the crack and previous to the OL position. This higher resolution provided sufficient data to understand Geometrical Necessary Dislocations (GND) distribution. Data acquisition and evaluation were managed using Oxford AZtec (version 3.3) and AZtecCrystal software.

- Phase Analysis (XRD): For phase identification, separate specimens were sectioned along three orthogonal planes relative to the build direction (transverse XY, longitudinal XZ, and YZ planes). Measurements were performed using a Bruker D8 DISCOVER (Málaga, Spain) diffractometer equipped with TRIO optics and a Cu Kα radiation source. Phase identification was achieved by a systematic comparison of the experimental diffraction peaks with reference patterns from the ICDD PDF-5 database.
- Nano-mechanical test (Nanoindentation): To assess localised mechanical properties and microstructural heterogeneity, nanoindentation mapping was carried out on the wrought baseline and the additively manufactured specimens, sectioned along three orthogonal planes relative to the build direction (transverse XY, longitudinal XZ, and YZ). A total of 50 points were measured for the wrought sample, and 120 points were measured for each of the three AM planes. Measurements were taken using a Micro Materials Ltd. NanoTest Platform 2 (Málaga, Spain), fitted with a standard Berkovich diamond indenter tip. Contact hardness (H_c) was extracted from the load–displacement curves.

3. Results and discussion

3.1. Microstructure, texture and phase characterisation

Given the highly anisotropic and heterogeneous microstructures inherent to the LPBF process, establishing a fundamental microstructural baseline is essential for interpreting the subsequent fatigue behaviour [2,43,57]. A porosity analysis based on 2D images is presented in Fig. 3. Fig. 3 (a) shows the porosity percentage for each plane. The XY plane, normal to the BD, exhibits lower porosity (0.040%) than the XZ and YZ planes (0.048%), which are parallel to the BD. Fig. 3(b) shows pore aspect ratio (f_{aspect}) plotted against circularity (f_{circ}) for each specimen plane. Marginal kernel density estimates accompany each axis to convey the distribution of points, in order to help visualisation of the local density. Because our maximum pore diameter (~25 μm) falls well below the minimum size thresholds for lack-of-fusion and keyhole defects established by Snell et al. [65], and the pores exhibit highly equiaxed shapes (f_{circ} mostly > 0.65 and f_{aspect} near 1), the defects can be classified predominantly as entrapped gas porosity. Overall, the detected mean pore diameter is in the order of 2 to 2.5 μm for all measured samples. Fig. 4 presents the XRD patterns for Wrought and As-Built AM Inconel 718 samples in three orthogonal directions, plotted on a logarithmic scale to address intensity disparities from crystallographic texture [66,67]. A direct comparison reveals severe crystallographic anisotropy in the AM material, absent in the Wrought condition.

While the Wrought sample exhibits a standard polycrystalline diffraction profile with a dominant γ reflection, the AM samples display a complete inversion of peak intensities depending on the sectioning plane. The AM X-Y plane (transverse cut) exhibits a suppression of the γ peak [68]. This confirms the expected strong ⟨001⟩ fibre texture parallel to the build direction, while the similar profiles of the Y-Z and X-Z planes indicate transverse isotropy [69]. Furthermore, the LPBF builds display broader and less-defined secondary phases — laves and *MC*/ $M_{23}C_6$ carbides — reflections than the wrought material, which is a direct consequence of rapid solidification-induced lattice microstrain and interdendritic segregation [70]. Although their low volume fraction (<5% [1]) prevents quantitative analysis, their detection confirms that the as-built microstructure retains significant brittle segregations distinguishing it from the Wrought condition [43].

Further characterisation is shown in Fig. 5, where Fig. 5(a) presents SEM micrographs of the etched AM IN718 samples along orthogonal planes. As expected, melting pool boundaries are clearly discernible, building up the layer-by-layer structure of the AM sample, with a spacing of 90 μm. Higher magnification views confirm the brittle segregations identified in the XRD profiles, Fig. 4, forming a cellular-dendritic substructure typical of rapid solidification kinetics [2,71,72].

The severe crystallographic anisotropy deduced from the XRD patterns is directly corroborated by the EBSD inverse pole figure (IPF) maps, Fig. 5(b–e). The 3D EBSD reconstruction, Fig. 5(b), visualises the competition between nucleation of fine grains within melt pools and the growth of massive columnar grains extending across multiple layers along the build direction (BD) [73]. The transverse X-Y plane reveals a "chessboard" grain pattern indicative of the orthogonal scanning strategy [74].

The IPF and pole figures shown in Fig. 5(c) and (d) corroborate the texture deduced from the XRD and shown in the EBSD. The AM samples display a pronounced columnar texture, with the < 001 > crystallographic direction aligned parallel to the BD [9,38,75]. In contrast to AM,

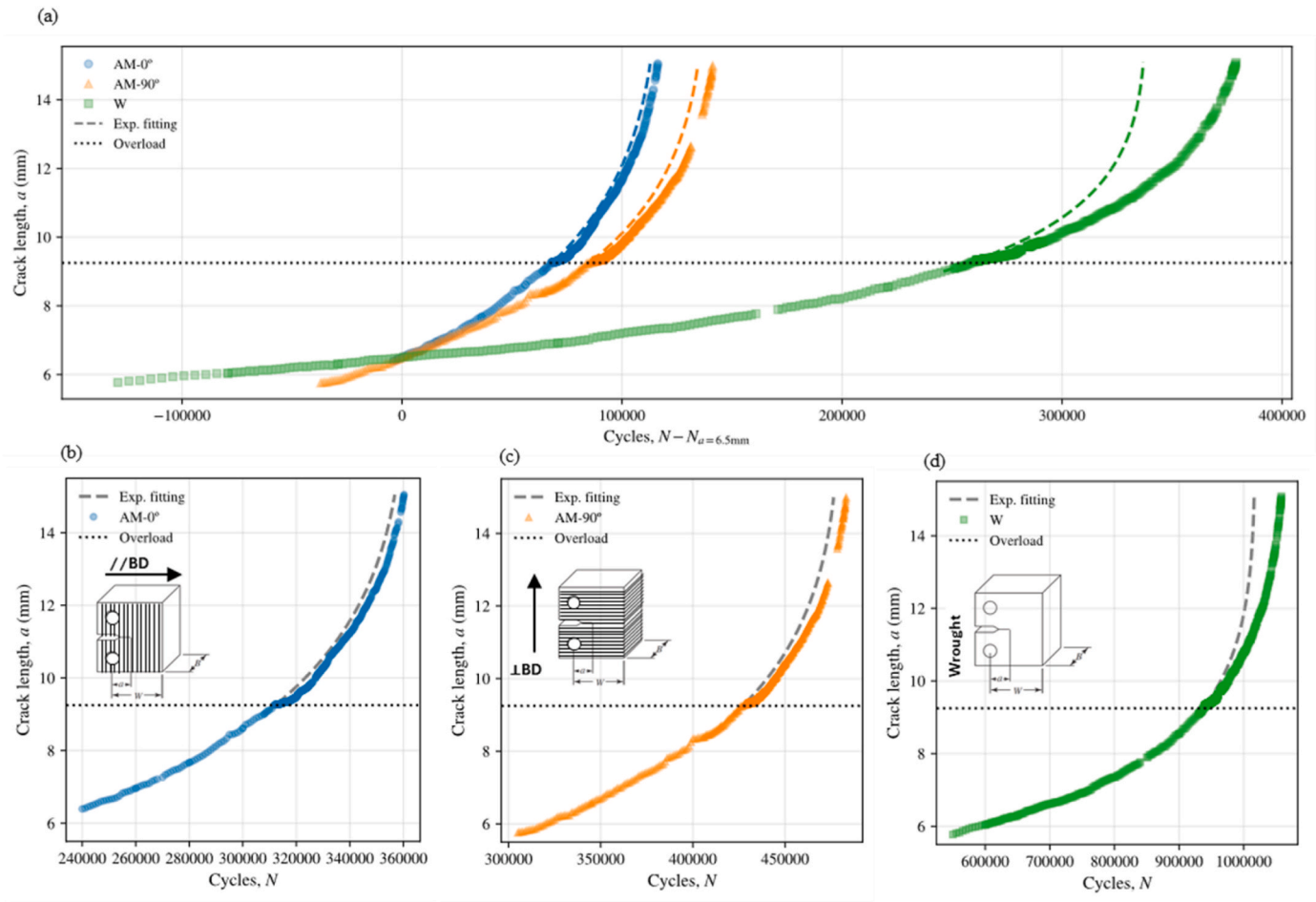


Fig. 7. Fatigue crack growth ($a - N$) curves for Wrought and As-Built AM Inconel 718. (a) Comparative growth behaviour normalised to $a = 6.5$ mm. (b-d) Absolute cycles for AM-0°, AM-90°, and Wrought samples. Experimental-fitted behaviour is represented by dashed lines and the OL event is marked by the dotted line.

the wrought material, Fig. 5(f), shows an evident isotropic orientation in the cross-section with a slight texture intensity along the forging direction, which is not even comparable to the AM anisotropy [15].

What is remarkable about the grain size in Fig. 5 is that, according to standard ASTM E112 measurements, the AM samples (G = 8.0–8.2) and the Wrought sample (G = 7.7) appear statistically similar. However, this average metric masks the morphological disparity seen in other works [69] and in the current results. The distribution histograms reveal that the AM microstructure follows a bimodal distribution with a high frequency of small, nucleated grains ($< 1,000\ \mu m^2$) that coexist with massive columnar grains, as seen in the IPF maps, reaching areas as large as $60,000\ \mu m^2$. Conversely, the wrought sample exhibits a unimodal distribution with grain areas consistently below $10,000\ \mu m^2$.

Fig. 6 presents the nanoindentation contact hardness (H_c) distributions for the wrought baseline and the AM IN718 specimens across the three orthogonal planes. The wrought material shows a relatively uniform hardness profile with a narrow data spread, consistent with a well-homogenised microstructure in which solid-solution strengtheners and fine precipitates are evenly distributed [1,70]. The AM planes, by contrast, all display a markedly lower median hardness alongside considerable microstructural heterogeneity, with standard deviations more than double those recorded for the wrought material. This lower median hardness in the AM specimens is consistent with a niobium-depleted γ matrix, a consequence of the rapid solidification rates inherent to the LPBF process, which limits the formation of strengthening γ″ precipitates [2,76]. A pronounced tail of high-hardness outliers is also evident in the AM data, reaching values of up to 100 GPa; these are attributed to indents that intersect the heavily segregated interdendritic cellular networks, where hard, brittle Laves phases and MC carbides are concentrated [75]. Notably, this micromechanical heterogeneity is present across all three planes (X-Y, X-Z and Y-Z), suggesting that although the bulk material may display macroscopic anisotropy, the localised features responsible for these hardness gradients is an inherent characteristic of the as-built condition. The transverse isotropy noted above is also reflected in the median H_c values: the X-Y plane (4.43 GPa) shows a higher hardness than the X-Z and Y-Z planes (4.10 and 4.12 GPa, respectively), which are, as expected, very similar to one another. This is consistent with the X-Z and Y-Z planes both containing the build direction, whereas the X-Y plane lies perpendicular to it.

3.2. Macroscopic fatigue crack growth kinetics

The fatigue crack growth behaviour is first evaluated in terms of crack length as a function of the number of cycles, followed by an analysis of crack growth rates and overload-induced transient effects. The first results of the fatigue performance are presented in Fig. 7 as crack length (a) versus number of cycles (N). The gaps in the plotted data are due to temporary interruptions in image acquisition during the experiment. In the pre-OL stage (6.5 mm $< a <$ 9.3 mm), the AM-0° orientation demonstrated the lowest resistance to crack propagation, reaching the overload point ($a \approx 9.3$ mm) in just 70,000 cycles. The AM-90° needs an additional set of 15,000 cycles (a ∼ 21% increase) to reach this point, while the wrought sample exhibited significantly higher damage tolerance, requiring nearly 285,000 cycles to cover the same crack extension. These results are in agreement with those obtained in

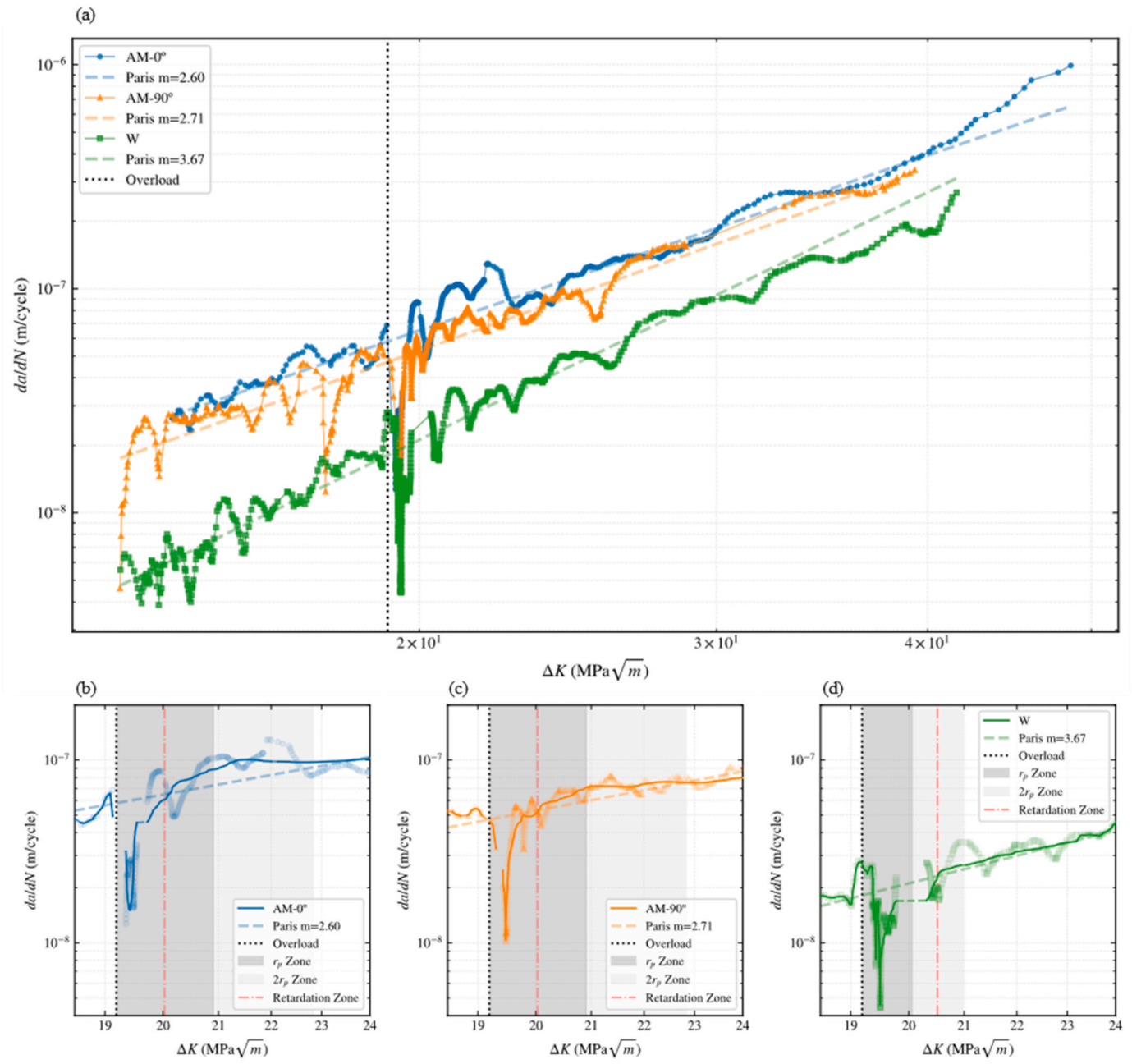


Fig. 8. (a) Fatigue crack growth rate (da/dN) vs. Stress Intensity Factor Range (ΔK). (b-d) Zoom in view of the OL region for AM-0°, AM-90° and Wrought samples respectively. The OL event is marked by the dotted line; the equivalent ΔK of the calculated plastic zone size (r_p and) is shaded in grey. End of obtained retardation zone is marked as a red vertical dashed dotted line. (For interpretation of the references to colour in this figure legend, the reader is referred to the Web version of this article.)

literature [9,75]. At $a \approx 9.3$ mm, a single 50% OL was applied, generating a deviation in crack growth rate from the expected trend (fitted from experimental data) in Fig. 5(b–d) for all samples.

To quantify the instantaneous crack growth response and the transient effects of the single overload (OL), the crack growth rate (da/dN) is plotted as a function of ΔK in Fig. 8. The high resolution of the optical tracking reveals a distinct "unsteady" or oscillatory growth behaviour, particularly in the pre-OL regime. A detail of these fluctuations is shown in Fig. 9, with decelerations of the crack growth rate coincident to crack asperities or deflections seen on micrographs of the C(T) surface where DIC images were taken. AM-0°, Fig. 9 (a), sample shows a moderate tortuosity, which results in less fluctuations. On the other hand, AM-90° and Wrought samples, Fig. 9(b) and (c), show a more prominent tortuosity with its consequent greater fluctuation on the crack growth rate [77]. The differences in the tortuosity of the samples are in line with the microstructure: while in AM-0° the columnar grains are aligned in the direction of the crack, in AM-90° the columnar structure is perpendicular to it, resulting in visibly greater tortuosity and, consequently, crack growth fluctuations. In the Wrought specimen, the crack deflects when it encounters equiaxed grains with high-angle grain boundaries or twins. These fluctuations became more evident given the high number of images and crack length measurements taken during the FCG test, an order of magnitude bigger than other recent studies [78,79].

The difference in FCG between Wrought and AM samples is prominent, with a moderate improvement in fatigue resistance of the AM-90° with respect to the AM-0° specimen. This improvement might initially

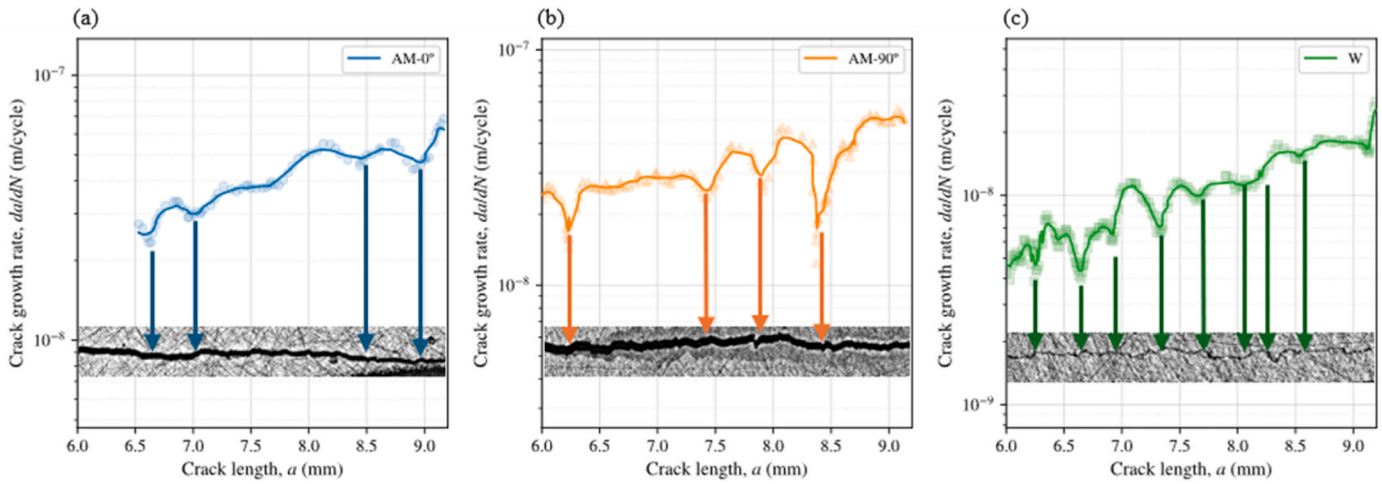


Fig. 9. Fluctuations of fatigue crack growth rate (da/dN) vs. Crack length (a) in the pre-OL region, for (a) AM-0°, (b) AM-90° and (c) Wrought samples respectively. Optical micrograph of the crack is superimposed at the same scale.

be attributed to the difference in porosity registered, Fig. 3 (a), in the XY plane (crack [78,79] plane for AM-90°) compared to the YZ plane (crack plane for AM-0°). However, although porosity has been reported to influence crack initiation (Region I) [15,80], no significant effect has been observed in the literature on the fatigue crack growth regime (Region II) for IN718 AM specimens [57,72]. As seen in Fig. 3(b), the pores detected are round, which are less severe stress concentrators than irregular or angular pores (like lack of fusion defects). An example of these pores can be seen in Fig. 15(a) in Section 3.4. Since they lack sharp features capable of producing strong local stress concentrations, it is expected to have little effect in the FCG. Therefore, the FCG difference between AM specimens is likely attributable to another source.

In order to account for the effect of the OL, the extent of the transient retardation zone—defined the crack growth distance from the overload application until the growth rate recovers to the baseline Paris trend—was evaluated. This retardation extent was then compared to the theoretical plastic zone, r_p, calculated using the softer yield strength (σ_{ys}) of 632 MPa for both AM cohorts [41], and 877 MPa for the equiaxed Wrought condition. The theoretical OL monotonic plastic zone sizes, $r_p = \frac{1}{\pi}\left(\frac{K_I}{\sigma_{YS}}\right)^2$, are calculated based on the second-order estimate of the Irwin's approximation [81]. While this isotropic calculation serves as a standard comparative baseline, its applicability to the highly textured AM microstructures is critically evaluated in Section 3.3.

Following the OL event, all samples exhibit immediate growth retardation, identifiable by the sharp drop in da/dN, Fig. 8(c and d). This retardation persists over a crack extension corresponding to half the theoretical r_p for AM-0° and AM-90° samples and around a 50% beyond the r_p for Wrought sample. The Wrought sample exhibits the strongest shielding effect, with the growth rate dropping by nearly an order of magnitude (from 2×10^{-5} to 4.5×10^{-6} mm/cycle). In contrast, the AM samples show a comparable, albeit milder, retardation magnitude. The crack growth rate recovery profile differs between manufacturing methods. The Wrought sample presents a recovery with intermediate fluctuations. Although the raw data show some oscillations that go beyond the Paris trend, the smoothed curve does not present an overshoot transition above the Paris trend. While the AM-0° shows some fluctuations, both AM samples follow a classic V-shape recovery. However, in contrast with the Wrought sample, they do show an acceleration of the growth rate above the Paris fit at approximately half the extent of the OL PZ, attributed to crack front curvature effects [82] and/or local crack-tip stress redistribution [83]. Regardless of the dominant mechanism, growth rates fully stabilise at twice the OL r_p.

For a distinct driving force (e.g., $\Delta K = 15$ MPa $\sqrt{m}$), both AM variants exhibit higher growth rates than the Wrought counterpart, driven by the higher Paris law intercept (C) associated with the AM microstructure (Table 3). AM anisotropy has been studied previously on LPBF IN718 [8], suggesting that build direction has negligible influence on the stable Paris region crack growth. However, the data in Fig. 8 reveals a distinct anisotropy, indicated by the consistent lower crack growth rates of the AM-90° orientation compared to the AM-0°. This implies that crack propagation perpendicular to the build layers—and thus perpendicular to the columnar grains—provides a slightly superior resistance to FCG. Ostergaard et al. [9] previously reported superior fatigue performance for AM-90° samples compared to the parallel orientation at ΔK levels below 20 MPa $\sqrt{m}$, something that is corroborated in Fig. 8 and further indicates that this performance advantage persists up to $\Delta K \approx 40$ MPa $\sqrt{m}$.

Table 3
Paris Law coefficients (C, m) for steady-state growth (excluding OL $2r_p$).

Sample	m_{nom}	C_{nom} (m/cycle·(MPa$\sqrt{\text{m}}$)$^{-m}$)
AM-0°	2.60	2.72E-11
AM-90°	2.69	1.70E-11
Wrought	3.67	3.57E-13

Table 3 summarises the Paris Law constants (C and m) derived from the steady-state regions (excluding two times the PZ size, $2r_p$, transient zones). The Wrought sample exhibits the highest slope ($m \approx 3.67$), yet its significantly lower intercept (C) ensures it maintains the lowest overall growth rate within the studied region. Among the AM samples, the AM-90° shows a slightly higher slope but lower intercept than the AM-0°, mathematically confirming its superior resistance in the tested range. Additionally, the AM-90° sample displays an anomalous deceleration at around 17.5 MPa$\sqrt{\text{m}}$. After surface inspection, this deceleration is attributed to a secondary crack propagating parallel to the main fracture plane, and to the building layers, at this exact position.

3.3. Macroscopic shielding and residual stress

Crack closure was quantified using DIC and COD data to explain the physical mechanisms driving the distinct FCG kinetics. Fig. 10 presents the evolution of the normalised opening level (K_{op}/K_{max}) as a function of crack length (a), with detailed magnifications of the overload (OL) transient region, Fig. 10(b–d).

In the pre-OL steady-state regime, the Wrought condition maintains a consistently higher closure level ($K_{op}/K_{max} \approx 0.5$) compared to the highly variable AM specimens (0.25 to 0.50). These results are in accord

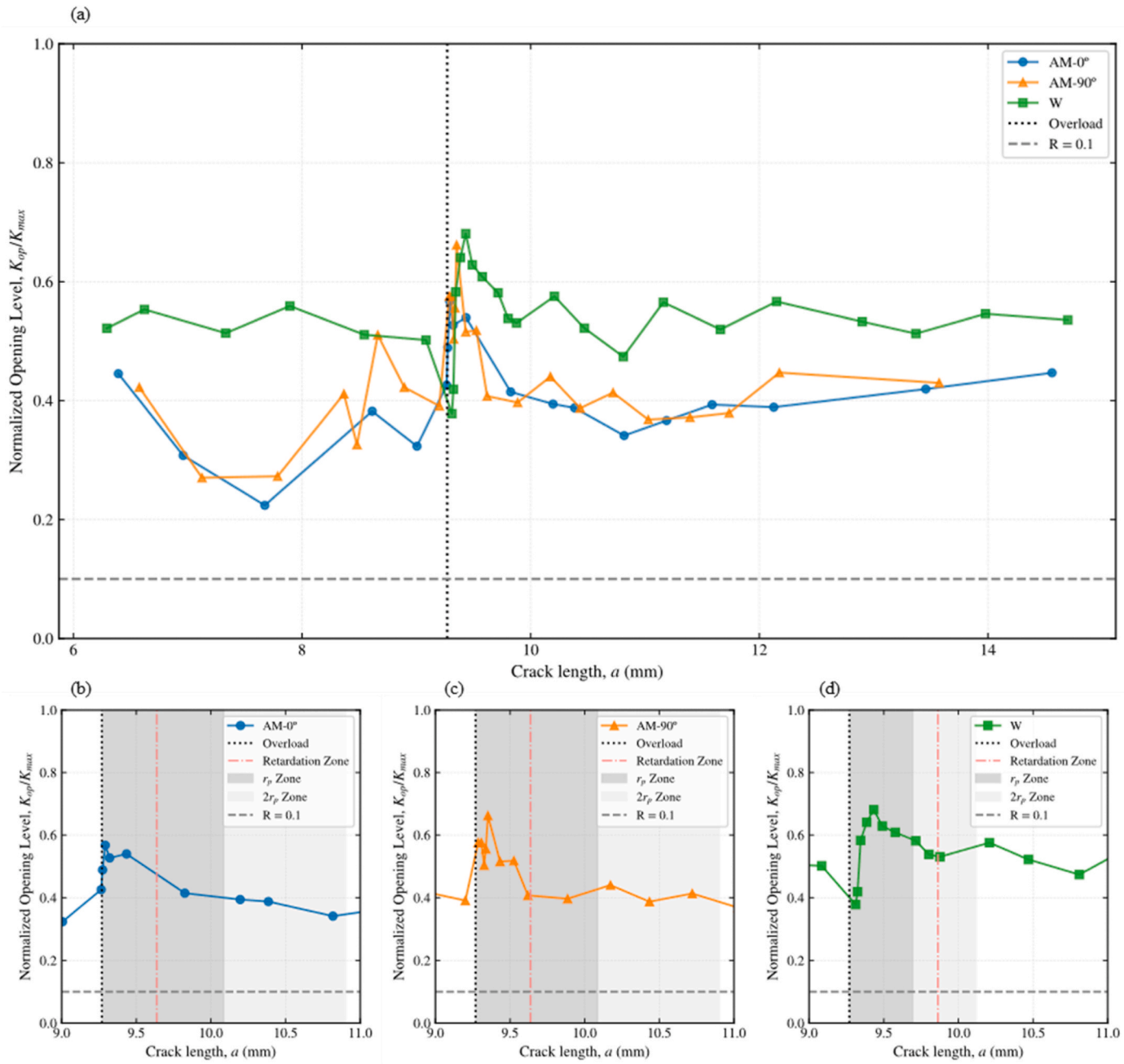


Fig. 10. (a) K_{op}/K_{max} – a chart for all samples. (b), (c) and (d) zoom in view of the OL region for AM-0°, AM-90° and Wrought samples respectively. OL event is represented with dot line, load ration, R, is represented with dash line and r_p and $2r_p$ zones are represented with grey zones. End of obtained retardation zone is marked as a red vertical dashed dotted line. (For interpretation of the references to colour in this figure legend, the reader is referred to the Web version of this article.)

with previous studies for both conventional and AM IN718. For the Wrought alloy, Andersson et al. [84] reported a mean closure level of 0.40, with localised peaks reaching 0.55 within $\sim 10\ \mu m$ of the crack tip. This aligns with the average closure before the OL, $K_{op}/\ K_{max} = 0.53$, and the transient overload peak of 0.64 measured. Additionally, the lower steady-state closure levels observed in the AM specimens, varying from 0.35 to 0.40, are highly consistent with the results of Wang et al. [19]. Their COD profiles for LPBF IN718 confirmed that crack closure occurring largely dissipate at driving forces exceeding 0.3 to the maximum force applied, validating the reduced macroscopic shielding capacity of the AM microstructure. This elevated closure in the wrought material proportionally reduces ΔK_{eff}, directly explaining its superior fatigue resistance and lower Paris law intercept (C) detailed previously (Table 3).

It is important to note that the C(T) dimensions fundamentally may influence crack tip constraint and the resulting crack closure levels. To quantitatively evaluate the geometric constraint in this study, the required thickness for a predominantly plane strain state was calculated using the standard ASTM E399 [53] criterion: $B \geq 2.5(K_{max}/\sigma_{YS})^2$. During the critical pre-overload phase and precisely at the peak of the 50% overload application ($a = 9.3$ mm, yielding a maximum applied stress intensity $K_{max} \approx 32.1\ \mathrm{MPa}\sqrt{\mathrm{m}}$), the minimum required thickness to maintain plane strain ranges from 3.35 mm for the high-strength wrought baseline to 6.44 mm for the lowest-strength AM-90° condition. Because all specimens utilised in this study possessed a uniform thickness of 6.0 mm, the crack tip operated under predominant plane

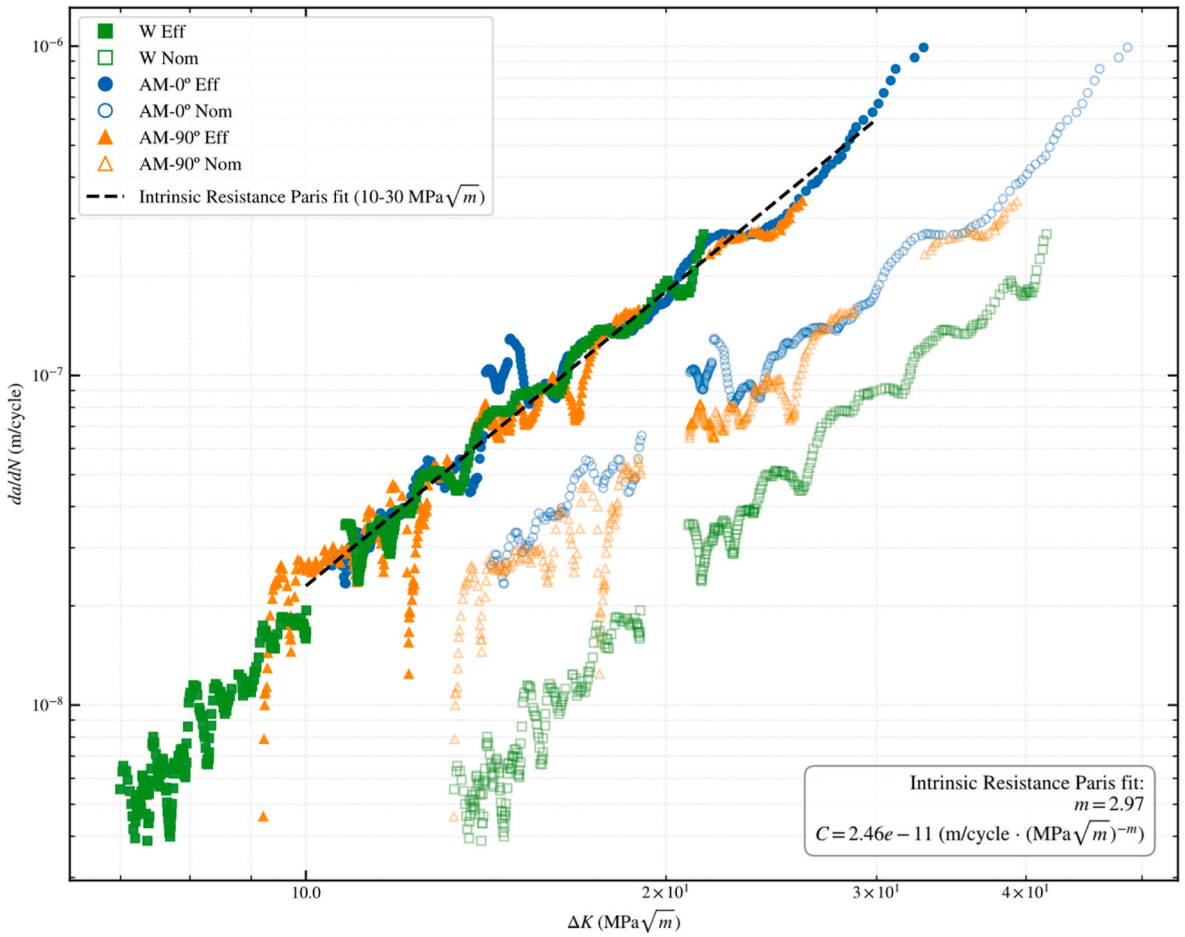


Fig. 11. Fatigue crack growth rate (da/dN) as a function of the nominal (ΔK, open symbols) and effective (ΔK_{eff}, solid symbols) SIF ranges. A Paris fit of the intrinsic material behaviour is added as a dashed black line, with its constants in the bottom right.

strain conditions for the Wrought and AM variants, maximising geometric constraint and limiting the free-surface PZ size. Consequently, the baseline values and the overload retardation behaviour observed in these tests are expected to be representative of thick-section and high-constraint conditions, with comparable results in FCG and closure anticipated in larger specimens provided the plane strain condition is satisfied [85].

Upon the application of the OL, the Wrought specimen exhibits an immediate drop in the K_{op}/K_{max} to approximately 0.40, nearly identical to the values observed in the AM variants prior to the OL. Following the initial crack tip blunting from the OL [86,87], a rapid rise in closure occurs due to PICC [5,27]. The magnitude of this PICC varies between materials but all of them are near a value of 0.60. The Wrought sample develops the strongest closure wake, peaking at $K_{op}/K_{max} = 0.68$, followed by the AM-90° (0.66) and the AM-0° (0.57).

Crucially, the spatial extent of this localised closure increase physically maps the macroscopic OL retardation zone. This zone reaches around 0.6 mm for the Wrought sample, surpassing its theoretical r_p boundary of 0.43 mm. This sustained PICC wake (~0.6 mm) directly correlates with the extended retardation zone observed in the crack growth rate curves, Fig. 8, whereas the truncated closure region in the AM specimens (~0.4 mm) results in earlier recovery of crack growth rates. In accordance with the present results, previous studies have demonstrated that this behaviour is characteristic of the wrought alloy's homogeneous, equiaxed microstructure, with OL retardation zones excessing the OL r_p [5,88,89]. Contrary to surpassing the r_p, the AM specimens exhibit a truncation of the closure effect. Despite possessing significantly larger theoretical r_p values (0.83 mm), the zone of elevated closure for both AM orientations spans only ~0.4 mm. As a result of this, the crack growth retardation is supressed earlier, persisting for only $\approx 0.5r_p$. This rather contradictory result may indicate that standard isotropic r_p calculations overestimate the generated shielding zone in LPBF IN718. Using an anisotropic framework to evaluate the plastic yielding helps to explain the spatial extent of the crack growth retardation. Xin et al. [90] developed an analytical formulation based on the Hill yield criterion [91]. This shows that orthotropic yielding depends on a decoupled tensor of longitudinal (X), transverse (Y), and shear (S) yield limits. Based on their analytical solutions, the PZ extension directly ahead of the crack tip ($\phi = 0°$) is only driven by the interaction between the normal crack-tip stress fields and their orthogonal yield limits, due to the disappearance of the local shear fields. The AM-0° and AM-90° specimens are an exact orthogonal rotation of the same columnar architecture. Therefore, their principal longitudinal and transverse yield limits (X and Y) swap positions in the Hill yield equation. This mathematical symmetry implies that the vertical amplitude of the plastic zone is very sensitive to the yield strength in the loading direction. However, the horizontal yield boundary along the crack propagation plane remains the same for both orientations under the same ΔK. Having in mind that the OL transient retardation zone is related to this horizontal extent of the PZ [92], this theoretical anisotropic framework provides a mechanistic explanation for why both AM architectures produced an identical ~0.4 mm closure wake, irrespective of their diverging macroscopic yield strengths. The closure data provides further explanation for the anomalous growth rate deceleration observed in the AM-90° sample prior to the OL (around $a = 8.5$ mm), Fig. 10(a).

Taking advantage of the previously calculated shielding effects, the

Table 4
Mean crack closure level.

Sample	Pre OL K_{op}/K_{max}	Post OL K_{op}/K_{max}
AM-0°	0.34	0.39
AM-90°	0.38	0.40
Wrought	0.53	0.54

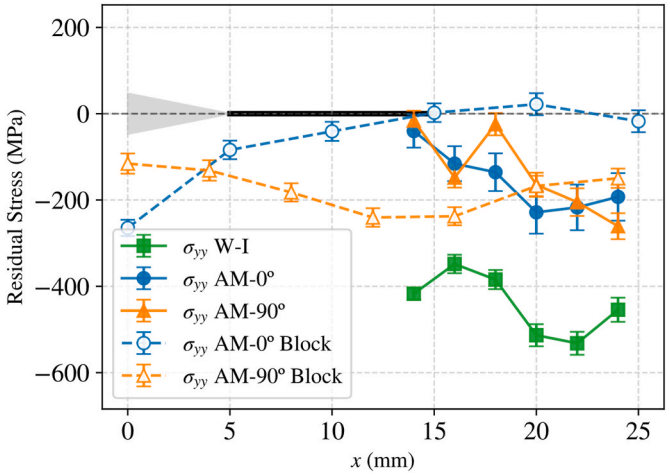


Fig. 12. Spatial distribution of residual stresses measured in the load direction (σ_{yy}). The pre-notch geometry and the physical extent of the fatigue crack are denoted by the grey triangle and the solid black line, respectively. The horizontal distance (x) is measured relative to the load-line ($x = 0$ mm) of the C(T) specimen.

FCGR were re-evaluated in terms of ΔK_{eff}. Following Elber's approach [81], the driving force is redefined by subtracting the closure contribution, such that $\Delta K_{eff} = K_{max} - K_{op}$. Fig. 11 presents the da/dN curves plotted against both the nominal (ΔK) and effective (ΔK_{eff}) driving forces, to isolate the intrinsic material resistance. For this analysis, a constant mean steady-state closure level (K_{op}/K_{max}) was applied. This mean value is calculated in two zones, previous and posterior to the OL, with values reported in Table 4. It should be noted that the use of mean K_{op} values simplifies the local variability of crack closure along the crack front and may not fully capture transient effects immediately after the OL, therefore the transient zone is not represented in Fig. 11.

When the extrinsic shielding is mathematically removed for all specimens, the da/dN curves shift to the left. The Wrought sample has a higher steady-state closure level (0.53) compared to the AM builds (~0.38). Because of this, its curve shows a much larger displacement to the left. This correction neutralises the performance gap seen in the nominal data, making the Wrought curve overlap with the AM data points in the stable Paris regime ($da/dN < 10^{-6}$ m/cycle). This overlap suggests that the intrinsic fatigue crack resistance of the IN718 is very similar in both cases, which agrees with other studies showing similar crack growth rates at higher load ratios [11]. As a result, the better fatigue performance of the Wrought condition (detailed in Section 3.2) is not caused by higher intrinsic fatigue crack resistance. Instead, it is mostly an extrinsic effect driven by its ability to maintain a strong closure wake (high K_{op}). Although, Table 4 shows small differences for the AM samples, the applied shift causes the curves to overlap. This helps explain the da/dN differences between the AM-0° and AM-90° orientations, mainly in the pre-OL region. Recent literature supports these findings as several studies have used ΔK_{eff}, including corrections for crack closure and residual stress, to show similar shielding effects in AM alloys [30–32]. The ΔK_{eff} curves shown in Fig. 11 further support the idea that porosity is not the primary factor behind the reduction in FCGR between the AM specimens, nor behind the difference between the wrought and AM specimens. Despite measurable differences in porosity between wrought and AM specimens, the ΔK_{eff} collapse indicates that closure-level differences account for the FCGR gap instead, as evidenced

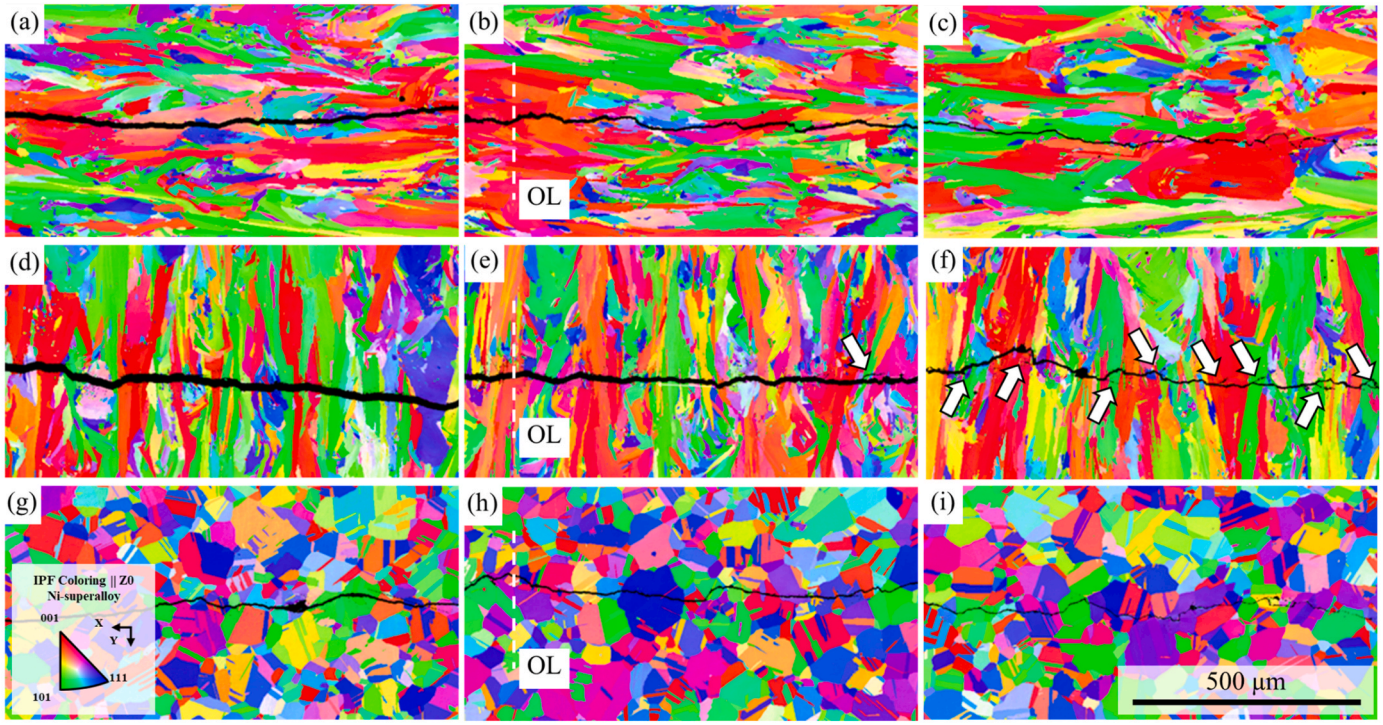


Fig. 13. EBSD inverse pole figure (IPF) maps tracking the crack propagation paths for the (a-c) AM-0°, (d-f) AM-90°, and (g-i) Wrought specimens. Columns represent crack lengths prior to the overload ($a = 8$ mm, $\Delta K \approx 17$ MPa$\sqrt{m}$), at the overload location, and post-overload ($a = 13$ mm, $\Delta K \approx 3$ MPa$\sqrt{m}$). The crack growth direction is from left to right. The AM-90° orientation displays severe secondary cracking and branching (white arrows).

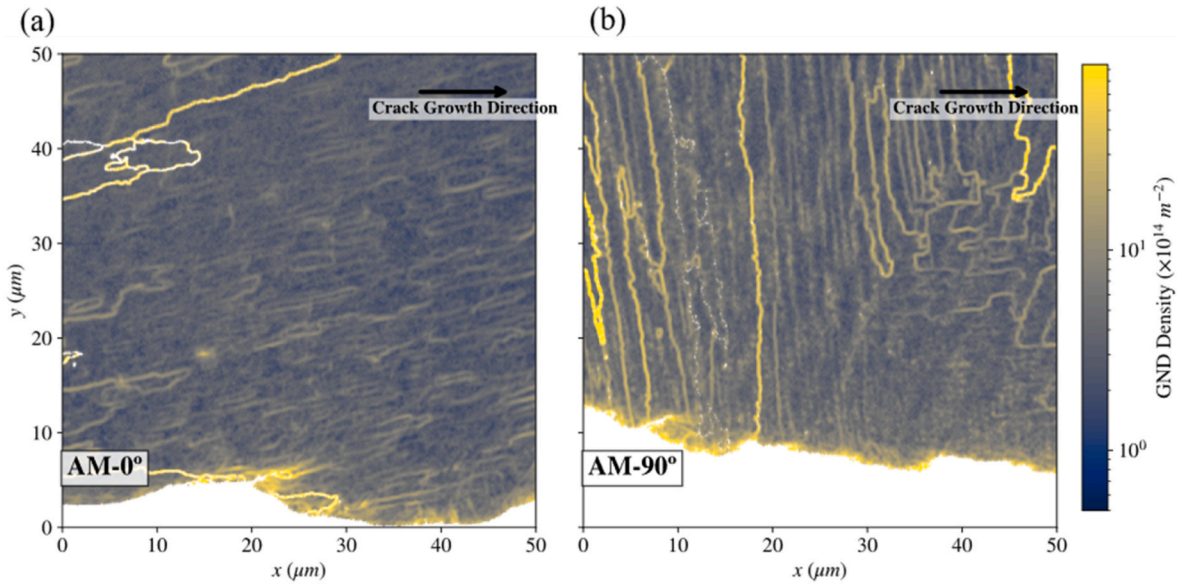


Fig. 14. GND Density maps for (a) AM-0° and (b) AM-90° in a position previous to the OL.

by the effective curves collapsing closely onto a single trend once adjusted for the closure levels measured at the specimen surface.

As a further step to investigate the impact of macroscopic shielding mechanisms, residual stress distributions were measured according to the scheme detailed in Fig. 2. Fig. 12 collects the load direction (σ_{yy}) residual stresses. As can be seen in Fig. 12, load direction stresses for Wrought specimen exhibits severe compression ranging from −350 to −550 MPa ahead of the crack tip. This strong compressive field creates a clamping force across the crack plane. This mechanical effect is the likely explanation for the high and stable closure levels shown in Section 3.3. Prior to testing, a strong compressive residual stress field exists in the AM-90° non-cracked block. Measurements show values from −100 to −250 MPa across the planned crack path. The AM-0° block, by comparison, starts in a nearly stress-free or slightly compressive state (around 0 to −100 MPa) within that same zone. Growing fatigue cracks create new fracture surfaces, which naturally relieve and redistribute

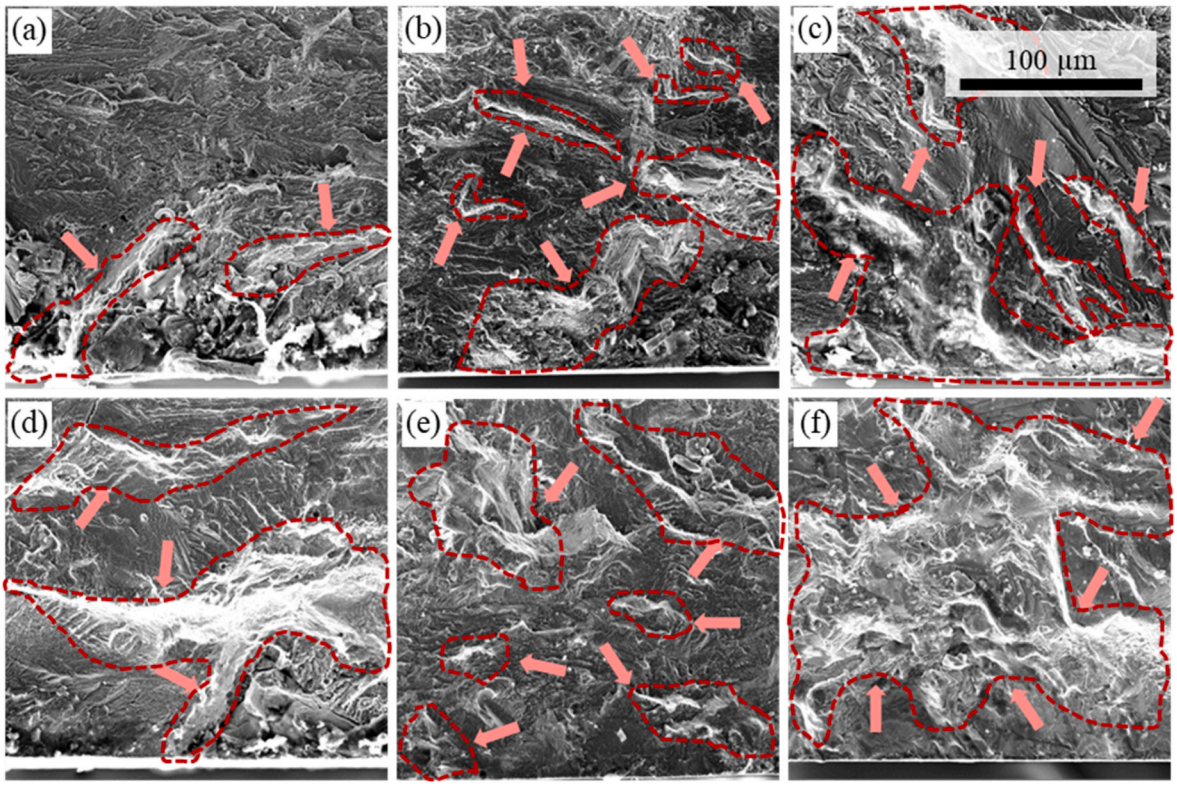


Fig. 15. High-magnification SEM fractographs acquired near the specimen free surfaces (bottom of images) for the (a, d) AM-0°, (b, e) AM-90°, and (c, f) Wrought samples. Images are categorised by low (a-c) and high (d-f) applied ΔK regimes. Red arrows highlight the varying morphologies of crack face abrasion, also localised inside dashed red lines. The macroscopic crack growth direction is from left to right. (For interpretation of the references to colour in this figure legend, the reader is referred to the Web version of this article.)

these starting stresses [93]. Thanks to this relaxation, post-test readings for both the AM-0° and AM-90° specimens end up at very similar compressive levels. They align between −50 and −250 MPa right in front of the stopped crack tip ($x \geq 14$ mm). The effect of the compression in the untested AM-90° block is clearly seen in Table 4, with crack closure data revealing and confirming this initial gap between AM samples. While the pre-OL closure magnitude for the AM-0° orientation is markedly lower than that of the AM-90° build, the post-OL values converge to a common baseline. This post-OL equilibration suggests a significant relief of internal residual stresses, mediated either by progressive crack wake extension or by the localised plasticity introduced during the overload event itself. Crucially, despite this stress relief in the crack wake, the actively advancing crack front in the AM-90° orientation was forced to continuously penetrate a pre-existing macroscopic compressive field. By continuously counteracting the applied far-field tensile loads during propagation, this inherent compression locally reduced the effective mean stress (R-ratio) at the crack tip [1,94], at least in the pre-OL part. It is widely acknowledged in the literature [5,95,96] that macroscopic compressive residual stresses act synergistically with PICC. Because PICC inherently manifests as a local field of compressive stresses within the plastic wake, the superposition of the bulk compressive stresses from the manufacturing process naturally amplifies this closure behaviour. Consequently, while this inherent compression unequivocally elevates the observed closure levels, its individual contribution cannot be entirely decoupled from the fundamental PICC or RICC mechanisms in the present research.

3.4. Crack path deflection and fractographic observations

EBSD maps, Fig. 13, along the crack wakes provide direct validation of the transient kinetics discussed in Section 3.2, confirming that crack growth behaviour depends on both crystallographic anisotropy and applied ΔK. Across all specimens, a transgranular fracture mode is mostly observed. However, the microstructure drives the local crack deflection. The Wrought material shows normal crack growth for a homogenised alloy, Fig. 13(g–i). The crack only deflects when it hits randomly oriented, equiaxed high-angle grain boundaries and internal annealing twins. This creates a moderate, even tortuosity that scales predictably with the driving force. AM samples behave quite differently as their columnar structure leads to severe micro-tortuosity that varies with orientation. Looking at the AM-0° orientation, Fig. 13(a–c), the main crack grows parallel to the long columnar grain boundaries. As the columnar boundaries align with the maximum principal stress plane, they provide an easier fracture path [19]. As a result, the crack in some AM-0° grains stops growing in a pure transgranular way, causing localised intergranular fractures and straight, fast-growing segments, Fig. 13(c). Conversely, the AM-90° crack front, Fig. 13(d–f) is forced to propagate perpendicularly across the elongated grain boundaries. Deflecting the crack 90° is highly difficult due to the energy needed for that, thus the crack must repeatedly cut through these obstacles. This interaction forces the crack to constantly shift its active crystallographic slip plane, resulting in a highly tortuous, zigzagging transgranular path [73]. This barrier effect gets greater at elevated driving forces ($\Delta K \approx 35\ \mathrm{MPa}\sqrt{m}$), Fig. 13(f), where the AM-90° specimen exhibits branching and secondary cracking, absent in the AM-0° and Wrought EBSD maps. At this stress intensity, the theoretical isotropic cyclic r_p expands to approximately 0.25 mm, which reaches multiple columnar grain boundaries. This high crack driving force derives in micro-cracks along the main crack path [97,98], Fig. 13(f). The observed crack deflection in the additively manufactured material is consistent with the columnar grain structure and crystallographic texture, which promotes anisotropic slip and contributes to variations in crack closure development.

To further clarify the microstructural constraints governing localised yielding behaviour, GND density maps were extracted from the 0.1 μm step EBSD datasets, Fig. 14, providing a direct spatial quantification of plastic strain accumulation near the crack, in a location previous to the OL. While the EBSD technique cannot discern other dislocation types from GNDs, it provides valuable insight into the spatial distribution of a portion of the total dislocations. A clear divergence in the dislocation arrangement is evident between the two additive orientations. The AM-0° specimen, Fig. 14 (a), exhibits regions of elevated GND density extending in horizontal direction, localised in the cellular structure seen along the grain crystallographic direction, being that parallel to the crack direction. This is consistent with easier plastic flow parallel to the longitudinal columnar grain boundaries [99]. The AM-90° specimen, Fig. 14 (b), in contrast, displays a more vertically distributed dislocation arrangement, as forward yielding is restricted by the perpendicular columnar boundaries, which act as strong barriers to dislocation motion [79,100]. Those dislocations are also arranged on the cell boundaries, perpendicular to the crack direction, in line with the direction of the crystallographic plane. This spatial variation in plastic strain accumulation lends direct microstructural support to the anisotropic Hill yielding behaviour discussed in Section 3.3. The orthogonal rotation of the columnar architecture alters the local principal yield limits, causing the AM-90° plastic zone to expand vertically while the AM-0° zone extends longitudinally. Notably, despite these morphological differences arising from building direction, the effective horizontal constraint responsible for the truncated overload retardation zones remains comparable between the two AM builds.

High-magnification SEM fractography near the specimen free surfaces, Fig. 15, provides direct physical validation for the crack closure mechanisms quantified in Section 3.3. Across all fractographies, the fracture surfaces exhibit clear localised fretting damage and abrasion, indicative of repeated crack face contact during the unloading portion of the fatigue cycles [101]. The morphology of these burnished regions, however, differs between materials. The wrought fracture, Fig. 15(c) and (f), display broad abrasion zones across planar facets, visually confirming the macroscopic PICC and compressive fields measured earlier. The strong compressive clamping along the full crack wake drives widespread rubbing between fracture surfaces. By contrast, wear patterns in the AM specimens are highly localised, Fig. 15(a), (b), (d) and (e). Instead of broad rubbing across the plane, characteristic of PICC [102], the abrasion highly concentrates on the peaks of surface asperities and microstructural steps for both the AM-0° and AM-90° builds. The observation of this localised fretting provides strong evidence that while both PICC and RICC are active, PICC is a stronger contributor to the closure mechanism in wrought material than in AM.

As the tortuous crack paths—driven by the orthogonal columnar grain boundaries—undergo mixed-mode microscopic displacements, the misaligned asperities prematurely contact during unloading [103]. This leaves discrete, highly concentrated abrasion marks strictly on the elevated fracture plane features. Notably, these closure signatures become increasingly prominent in the high-ΔK regime, Fig. 15(d–f). The amplified severity of this abrasion indicates a volumetric expansion of the active contact zones, driven by the naturally enlarged forward PZ at elevated driving forces an in line with the increase of the crack closure in Table 4. Further high-magnification SEM fractographic analysis reveals a driving-force-dependent transition in the active crack propagation micro-mechanisms, fully consistent with observations reported in the literature for both conventional and AM Inconel 718 [1,8,84,104]. At low ΔK before the OL ($12 - 19\ \mathrm{MPa}\sqrt{m}$), propagation is dominated by crystallographic slip along preferential planes, evidenced by a faceted basketweave morphology with scarce fatigue striations [8]. As the driving force increases, a mixed-mode regime emerges, before continuum ductile mechanisms become dominant in the upper Paris regime, marked by well-defined fatigue striations across all samples. Notably, the AM-90° specimen additionally develops prominent longitudinal tear ridges at elevated driving forces [1], consistent with the severe out-of-plane secondary cracking and macroscopic branching previously identified via EBSD mapping (Section 3.4).

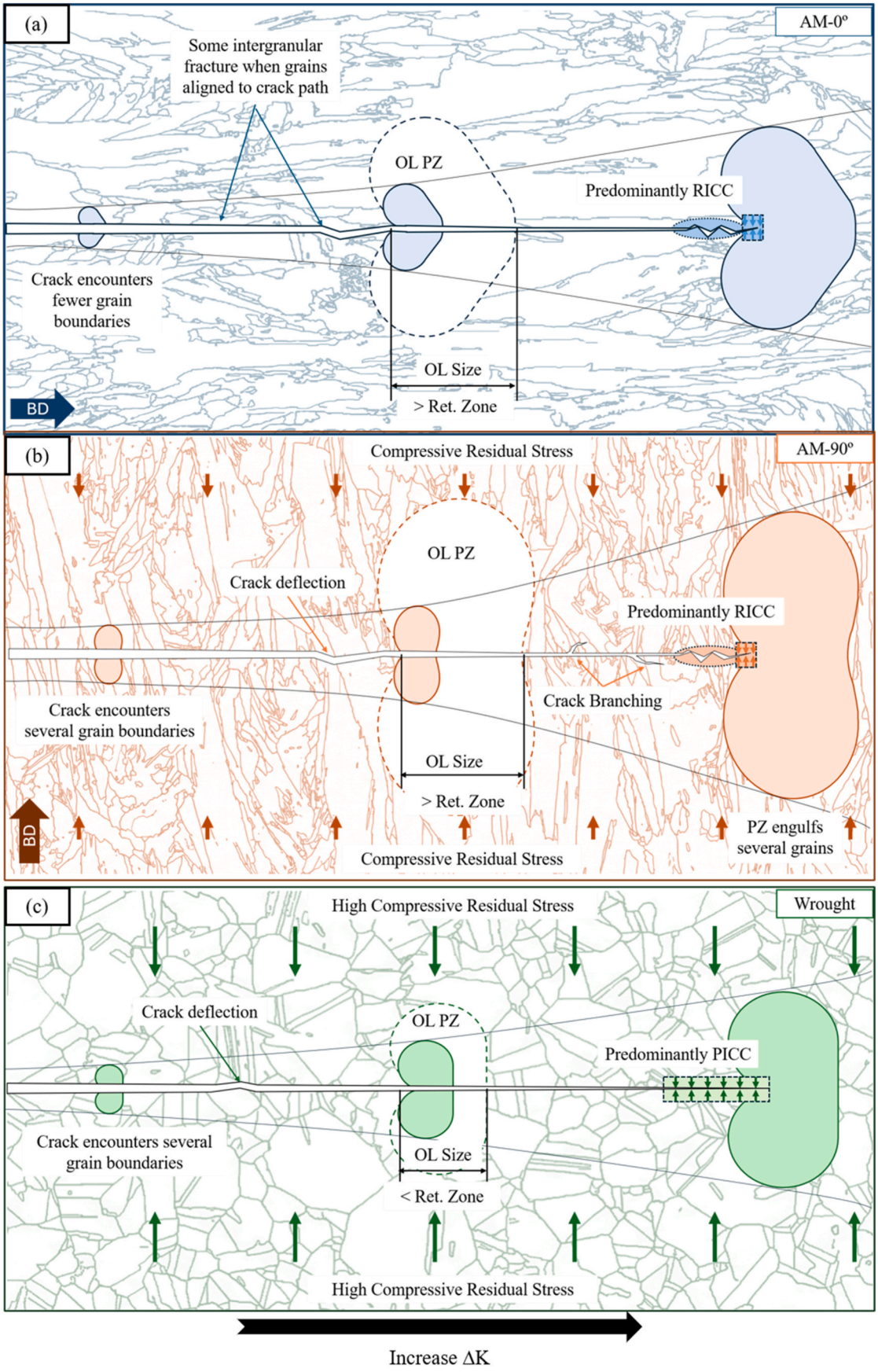


Fig. 16. Summary of FCG mechanisms in (a) AM-0°, (b) AM-90° and (c) Wrought samples.

3.5. Synthesis of anisotropic FCG and overload retardation mechanisms

To bring together the microstructural, kinematic, and fractographic observations discussed above, the governing mechanisms controlling fatigue crack growth (FCG) and overload-induced retardation are synthesised schematically in Fig. 16. This summary highlights the fundamental difference in damage mechanics between the strongly anisotropic LPBF architectures and the equiaxed wrought microstructure:

i. *AM-0° (parallel propagation)*. As shown in Fig. 16(a), crack propagation parallel to the LPBF build direction encounters few microstructural barriers, with a transgranular fracture path that occasionally follows grain boundaries, becoming intergranular where the crack front aligns in the same direction than the grain boundary. Because plastic yielding is strongly constrained in the transverse direction by the orthogonal yield limits (Hill criterion), the retardation zone induced by the overload is considerably smaller than the theoretical continuum estimate of r_p, resulting in a markedly truncated retardation zone (~0.4 mm). Shielding is predominantly governed by localised RICC at discrete asperity contacts rather than global PICC, as observed in the fractography.

ii. *AM-90° (transverse propagation)*. When forced to propagate perpendicular to the columnar build direction, Fig. 16(b), the crack repeatedly cuts across grain-boundary barriers (transgranular fracture), producing occasional crack path deflections at low SIF ranges and crack branching at high SIF ranges, with the increase of the PZ with respect to the grain size. Localised RICC due to asperity mismatch on unloading is also observed. Despite its lower macroscopic yield strength relative to the AM-0° orientation, the AM-90° specimen is subject to the same constrained yield limit along the crack propagation direction. As reflected in the comparable yielding ellipses in Fig. 16(a) and (b), this shared constraint results in a retardation zone length (~0.4 mm) essentially identical to that of the AM-0° build.

iii. *Wrought baseline (isotropic propagation)*. By contrast, as shown in Fig. 16(c), crack propagation through the randomly oriented, equiaxed wrought matrix occurs by transgranular fracture with moderate boundary deflection. The high monotonic yield strength and isotropic plasticity of the matrix mean that crack-wake shielding is dominated globally by PICC, reflected in broad compressive residual stress fields and widespread abrasion facets. Following the OL, the resulting plastic deformation produces an extended retardation zone (>0.6 mm) that exceeds the theoretical monotonic plastic zone size (r_p).

Overall, this summary indicates that while LPBF build orientation seems to affect both the crack path and the vertical extent of the PZ, the spatial extent of overload-induced retardation is governed primarily by the anisotropic constraints imposed on the horizontal extent of the OL PZ at the studied R_{OL}.

4. Conclusions

The fatigue crack growth kinetics and overload-induced retardation mechanisms of Laser Powder Bed Fusion (LPBF) Inconel 718 relative to its wrought counterpart has been assessed thoroughly. This study has identified the following principal conclusions:

- Within the scope of the tested specimens, the wrought IN718 alloy exhibits superior nominal FCG resistance compared to the as-built AM variants. Within the LPBF material, a moderate orientation dependence: crack propagation transverse to the build direction (AM-90°) showed slightly greater resistance than propagation parallel to it (AM-0°).
- Despite the microstructural anisotropy, both AM architectures exhibited highly comparable crack growth retardation distances of ~0.4 mm following a 50% tensile OL. Theoretical approximations suggest this orientation-independent transient behaviour is governed by the geometrically constrained horizontal extension of the plastic zone under orthotropic yielding.
- The data suggests that the enhanced nominal performance of the wrought material is primarily driven by its potent extrinsic shielding capacity. Upon normalising the kinetic data to the ΔK_{eff}, the crack growth curves converged, implying that the intrinsic crack propagation resistance is comparable across the tested microstructures.
- The application of a single OL induces immediate crack growth retardation across all microstructural conditions. However, while the wrought material sustains a prolonged retardation phase extending beyond Irwin's plastic zone, both AM build orientations exhibit a similar but severely truncated response. This suggests that standard isotropic models may significantly overestimate the effective shielding zone in as-built LPBF IN718.
- Fractographic and DIC observations indicate that the shielding in the wrought alloy relies on global PICC and strong compressive residual stresses. Conversely, closure in the analysed AM microstructures appears to be predominantly driven by RICC, facilitated by localised fretting against rigid columnar boundaries. Specifically, the 90° crack front advancing across these boundaries induced localised deflections and branching that impeded propagation.

CRediT authorship contribution statement

J.A. Aguilera: Conceptualization, Data curation, Formal analysis, Investigation, Methodology, Software, Validation, Writing – original draft, Writing – review & editing. **P.M. Cerezo:** Data curation, Investigation, Methodology, Writing – review & editing. **A.S. Cruces:** Conceptualization, Methodology, Project administration, Supervision, Writing – review & editing. **T. Guraya:** Conceptualization, Funding acquisition, Investigation, Resources, Writing – review & editing. **F. Paysan:** Conceptualization, Formal analysis, Methodology, Resources, Validation, Writing – review & editing. **J. Gussone:** Conceptualization, Formal analysis, Investigation, Resources, Validation, Writing – review & editing. **E. Breitbarth:** Conceptualization, Investigation, Project administration, Supervision, Validation, Writing – review & editing. **P. Lopez-Crespo:** Conceptualization, Funding acquisition, Investigation, Methodology, Project administration, Resources, Validation, Writing – review & editing.

Declaration of competing interest

The authors declare the following financial interests/personal relationships which may be considered as potential competing interests: P. Lopez-Crespo reports financial support was provided by Junta de Andalucia. P. M. Cerezo reports financial support was provided by Spanish Ministry of Science and Innovation. J. A. Aguilera reports financial support was provided by Banco Santander. P. Lopez-Crespo reports article publishing charges was provided by Universidad de Malaga CBUA. If there are other authors, they declare that they have no known competing financial interests or personal relationships that could have appeared to influence the work reported in this paper.

Acknowledgements

This research is supported by “FEDER Programa Operativo” by “Junta de Andalucía" (Spain) – grant reference UMA18-FEDERJA-250 and by an FPU grant (Formación de Profesorado Universitario) from the Spanish Ministry of Science and Innovation (MCINN) to P.M.C. (FPU23-03834). This research is supported by “Banco Santander” grant through the “Plan Propio Integral de Docencia de la Universidad de Málaga”. Authors would also like to acknowledge funding for open

access charge: Universidad de Malaga/CBUA.

Data availability

Data will be made available on request.

References

[1] S. Ghorbanpour, S. Sahu, K. Deshmukh, E. Borisov, T. Riemslag, E. Reinton, V. Bertolo, Q. Jiang, A. Popovich, A. Shamshurin, M. Knezevic, V. Popovich, Effect of microstructure induced anisotropy on fatigue behaviour of functionally graded Inconel 718 fabricated by additive manufacturing, Mater. Charact. 179 (2021) 111350.

[2] E. Hosseini, V.A. Popovich, A review of mechanical properties of additively manufactured Inconel 718, Addit. Manuf. 30 (2019) 100877.

[3] D. Gustafsson, E. Lundström, High temperature fatigue crack growth behaviour of Inconel 718 under hold time and overload conditions, Int. J. Fatigue. 48 (2013) 178–186.

[4] Z. Kang, X. Wang, Z. Wang, D. Zhou, T. Zhang, J. Wen, C. Zhang, J. Tang, J. Gong, Cyclic response and residual life prediction of Inconel 718 superalloy after overloading under hybrid stress-strain controlled creep-fatigue loading, Eng. Fail. Anal. 162 (2024) 108427.

[5] E. Salvati, H. Zhang, K.S. Fong, X. Song, A.M. Korsunsky, Separating plasticity-induced closure and residual stress contributions to fatigue crack retardation following an overload, J. Mech. Phys. Solid. 98 (2017) 222–235.

[6] C. Simpson, S. Kozuki, P. Lopez-Crespo, M. Mostafavi, T. Connolley, P. Withers, Quantifying fatigue overload retardation mechanisms by energy dispersive X-ray diffraction, J. Mech. Phys. Solid. 124 (2019) 392–410.

[7] X. Huang, L. Wang, Y. Hu, G. Guo, D. Salmon, Y. Li, W. Zhao, Fatigue crack propagation behavior of Ni-based superalloys after overloading at elevated temperatures, Prog. Nat. Sci. Mater. Int. 26 (2016) 197–203.

[8] S. Kim, H. Choi, J. Lee, S. Kim, Room and elevated temperature fatigue crack propagation behavior of Inconel 718 alloy fabricated by laser powder bed fusion, Int. J. Fatigue. 140 (2020) 105802.

[9] H.E. Ostergaard, J.D. Pribe, M. Tarik Hasib, A.M. Paradowska, T. Siegmund, J. J. Kruzic, Near-threshold fatigue crack growth in laser powder bed fusion produced alloy 718, Int. J. Fatigue. 163 (2022) 107041.

[10] J.D. Pribe, H.E. Ostergaard, T. Siegmund, J.J. Kruzic, Transient creep-fatigue crack growth in creep-brittle materials: application to Alloy 718, Fatigue. Fract. Eng. Mater. Struct. 45 (2022) 2873–2889.

[11] R. Jones, A. Ang, D. Peng, V.K. Champagne, A. Michelson, A. Birt, Modelling crack growth in additively manufactured Inconel 718 and Inconel 625, Metals 2023 13 (2023) 1300. Page 1300 13.

[12] M.M. Mirsayar, A generalized criterion for fatigue crack growth in additively manufactured materials – build orientation and geometry effects, Int. J. Fatigue. 145 (2021) 106099.

[13] S.A. Paluskiewicz, S.B. Narasimhachary, S.R. Shinde, C. Kain, Z.B. Towner, C. L. Muhlstein, Crack closure of Ni-based superalloy 718 at high negative stress ratios, Int. J. Fatigue. 160 (2022) 106822.

[14] L. Jacobsson, C. Persson, S. Melin, SEM study of overload effects during fatigue crack growth using an image analysing technique and potential drop measures, Fatigue. Fract. Eng. Mater. Struct. 33 (2010) 105–115.

[15] S. Park, Y. Tanaka, S. Okazaki, Y. Funakoshi, H. Kawashima, H. Matsunaga, Inferior fatigue resistance of additively-manufactured Ni-based superalloy 718 and its dominating factor, Int. J. Fatigue. 176 (2023) 107801.

[16] D. Xie, W. Zhang, Z. Lyu, P.K. Liaw, H. Tran, H.B. Chew, Y. Wei, Y. Ren, Y. Gao, Plastic anisotropy and twin distributions near the fatigue crack tip of textured Mg alloys from in situ synchrotron X-ray diffraction measurements and multiscale mechanics modeling, J. Mech. Phys. Solid. 165 (2022) 104936.

[17] K. Solberg, F. Berto, The effect of defects and notches in quasi-static and fatigue loading of Inconel 718 specimens produced by selective laser melting, Int. J. Fatigue. 137 (2020) 105637.

[18] R. Pippan, A. Hohenwarter, Fatigue crack closure: a review of the physical phenomena, Fatigue. Fract. Eng. Mater. Struct. 40 (2017) 471–495.

[19] Q. Wang, R. Bao, B. Liu, S. Lu, H. Peng, B. Chen, Comparison of fatigue crack growth behaviour in electron-beam and laser powder-bed-fusion Inconel 718, Mater. Sci. Eng., A 893 (2024) 146109.

[20] A. Anuar, T. Guraya, Z.W. Chen, M. Ramezani, M. San Sebastián-Ormazabal, Effect of build direction dependent grain structure on fatigue crack growth of biomedical Co–29Cr–6Mo alloy processed by laser powder bed fusion, J. Mech. Behav. Biomed. Mater. 123 (2021) 104741.

[21] J. Tong, Full-field characterisation of crack tip deformation and fatigue crack growth using digital image correlation—a review, Fatig. Fract. Eng. Mater. Struct. 41 (2018) 1855–1869.

[22] S.J. O'Connor, D. Nowell, K.I. Dragnevski, Measurement of fatigue crack deformation on the macro- and micro-scale: uniform and non-uniform loading, Int. J. Fatigue. 89 (2016) 66–76.

[23] J. Carroll, C. Efstathiou, J. Lambros, H. Sehitoglu, B. Hauber, S. Spottswood, R. Chona, Investigation of fatigue crack closure using multiscale image correlation experiments, Eng. Fract. Mech. 76 (2009) 2384–2398.

[24] J.D. Carroll, W. Abuzaid, J. Lambros, H. Sehitoglu, High resolution digital image correlation measurements of strain accumulation in fatigue crack growth, Int. J. Fatigue. 57 (2013) 140–150.

[25] W. Zhang, L. Cai, D. Zhou, F. Sun, In-situ microscopy testing of plasticity variation ahead of fatigue crack tip in AL2024-T3, Int. J. Fract. 216 (2019) 59–70.

[26] F. Paysan, D. Melching, E. Breitbarth, Advanced crack tip stress analysis using interaction integrals in high-resolution digital image correlation fields, Theor. Appl. Fract. Mech. 143 (2026) 105489.

[27] D. Nowell, P.F.P. de Matos, Application of digital image correlation to the investigation of crack closure following overloads, Procedia Eng. 2 (2010) 1035–1043.

[28] F. Paysan, D. Melching, E. Breitbarth, Plasticity-induced crack closure identification during fatigue crack growth in AA2024-T3 by using high-resolution digital image correlation, Int. J. Fatigue. 192 (2025) 108703.

[29] E. Wolf, Fatigue crack closure under cyclic tension, Eng. Fract. Mech. 2 (1970) 37–45.

[30] S. Hasunuma, M. Tsuruta, Y. Tomomasa, N. Sakaguchi, T. Hayase, Fatigue crack growth characteristics of additive-manufactured aluminum alloys based on the effective stress intensity factor range, Mechanical Engineering Letters 11 (2025) 25–83.

[31] C.M. Smudde, C.R. D'Elia, C.W. San Marchi, M.R. Hill, J.C. Gibeling, The influence of residual stress on fatigue crack growth rates of additively manufactured Type 304L stainless steel, Int. J. Fatigue. 162 (2022) 106954.

[32] C.M. Smudde, C.C. San Marchi, M.R. Hill, J.C. Gibeling, The influence of residual stress on fatigue crack growth rates in stainless steel processed by different additive manufacturing methods, J. Mater. Eng. Perform. 33 (2024) 7703–7713.

[33] T. Nicholas, G.K. Haritos, R.L. Hastie, K. Harms, The effects of overloads on sustained-load crack growth in a nickel-base superalloy: part II—Experiments, Theor. Appl. Fract. Mech. 16 (1991) 51–62.

[34] T. Nicholas, G.K. Haritos, R.L. Hastie, K. Harms, The effects of overloads on sustained-load crack growth in a nickel-base superalloy: part I—Analysis, Theor. Appl. Fract. Mech. 16 (1991) 35–49.

[35] Y. Alyousif, E.A. Saunders, S. Taylor, J.C. Walker, P.A.S. Reed, Slip mode transitions and work hardening of a polycrystalline superalloy: effects on striation Formation at room temperature, Fatigue. Fract. Eng. Mater. Struct. 49 (2026) 52–61.

[36] E. Storgärds, J. Saarimäki, K. Simonsson, S. Sjöström, D. Gustafsson, T. Månsson, J. Moverare, Scatter in dwell time cracking for a Ni-Based superalloy in combination with overloads, in: Volume 7A: Structures and Dynamics, American Society of Mechanical Engineers, 2015.

[37] J. Saarimäki, J. Moverare, R. Eriksson, S. Johansson, Influence of overloads on dwell time fatigue crack growth in Inconel 718, Mater. Sci. Eng., A 612 (2014) 398–405.

[38] S. Ghorbanpour, K. Deshmukh, S. Sahu, T. Riemslag, E. Reinton, E. Borisov, A. Popovich, V. Bertolo, Q. Jiang, M.T. Sanchez, M. Knezevic, V. Popovich, Additive manufacturing of functionally graded inconel 718: effect of heat treatment and building orientation on microstructure and fatigue behaviour, J. Mater. Process. Technol. 306 (2022) 117573.

[39] ASTM B311 - Test Method for Density of Powder Metallurgy (PM) Materials Containing less than Two Percent Porosity, 2017.

[40] R.F. Muraca, J.S. Whittick, NTRS - Materials Data Handbook: Inconel Alloy 718, 1972.

[41] Renishaw, Renam 500 Series Material Data Sheet - IN718, 2024.

[42] J. Schröder, A. Evans, E. Polatidis, J. Čapek, G. Mohr, I. Serrano-Munoz, G. Bruno, Understanding the impact of texture on the micromechanical anisotropy of laser powder bed fused Inconel 718, J. Mater. Sci. 57 (2022) 15036–15058.

[43] G. Kasperovich, J. Gussone, G. Requena, N. Schell, A. Stark, J. Haubrich, Tailoring the strength of inconel 718: insights into LPBF parameters and heat treatment synergy, Mater. Des. 250 (2025) 113627.

[44] Z. Xu, J.W. Murray, C.J. Hyde, A.T. Clare, Effect of post processing on the creep performance of laser powder bed fused Inconel 718, Addit. Manuf. 24 (2018) 486–497.

[45] S. Choudhary, A. Pandey, V. Gaur, Role of microstructural phases in enhanced mechanical properties of additively manufactured IN718 alloy, Mater. Sci. Eng., A 862 (2023) 144484.

[46] B. Liu, Y. Ding, J. Xu, Y. Gao, X. Wang, H. Zhang, Y. Hu, F. Sun, Outstanding strength-ductility synergy in Inconel 718 superalloy via laser powder bed fusion and thermomechanical treatment, Addit. Manuf. 67 (2023) 103491.

[47] N. Li, C. Wang, C. Li, Microstructures and high-temperature mechanical properties of inconel 718 superalloy fabricated via laser powder bed fusion, Materials 17 (2024) 3735.

[48] ASTM E8/E8M-22: Test Methods for Tension Testing of Metallic Materials, 2022.

[49] ASTM E647-24, Test Method for Measurement of Fatigue Crack Growth Rates, 2024.

[50] Y. He, K. Yuan, Y. Li, S. Zhao, D. Li, W. Guo, Overload-induced anisotropy of fatigue crack growth in laser deposited Ti–6Al–4V alloy, J. Mater. Res. Technol. 30 (2024) 6003–6016.

[51] D. Deng, R.L. Peng, J. Moverare, On the dwell-fatigue crack propagation behavior of a high strength superalloy manufactured by electron beam melting, Mater. Sci. Eng., A 760 (2019) 448–457.

[52] D. Deng, R.L. Peng, J. Moverare, A comparison study of the dwell-fatigue behaviours of additive and conventional IN718: the role of dislocation substructure on the cracking behaviour, Mater. Sci. Eng., A 797 (2020) 140072.

[53] ASTM E399-22, Test Method for Linear-Elastic Plane-Strain Fracture Toughness of Metallic Materials, 2022.

[54] A. Shaji Karapuzha, T. Wegener, M. Krochmal, Y. Zhu, T. Niendorf, D. Fraser, X. Wu, A. Huang, Fatigue crack growth in additively manufactured Hastelloy X - Influences of crack orientation and post-fabrication treatments, Mater. Sci. Eng., A 854 (2022) 143773.

[55] G. Wang, M. Zhang, Y. Fu, H. Zhang, W. Zhai, Y. Lu, R. Li, Isotropy of fatigue crack growth in hybrid additive manufactured Ti6Al4V ELI titanium alloy, Mater. Sci. Eng., A 909 (2024) 146850.
[56] A.G. Spangenberger, Y. Zhai, E.J. Brown, G.N. Vigilante, D.A. Lados, Fatigue crack growth behavior and microstructural mechanisms at room and elevated temperatures in Inconel 718 manufactured by laser engineered net shaping, Mater. Sci. Eng., A 965 (2026) 150337.
[57] M. Prost, A. Köster, D. Missoum-Benziane, S. Dépinoy, L. Ferhat, M. Rambaudon, V. Maurel, Anisotropy in cyclic behavior and fatigue crack growth of IN718 processed by laser powder bed fusion, Addit. Manuf. 61 (2023) 103301.
[58] P. Miarka, A.S. Cruces, S. Seitl, L. Malíková, P. Lopez-Crespo, Influence of the constraint effect on the fatigue crack growth rate in S355 J2 steel using digital image correlation, Fatigue. Fract. Eng. Mater. Struct. 43 (2020).
[59] D. Camas, P. Lopez-Crespo, A. Gonzalez-Herrera, B. Moreno, Numerical and experimental study of the plastic zone in cracked specimens, Eng. Fract. Mech. 185 (2017) 20–32.
[60] T. Strohmann, D. Melching, F. Paysan, A. Klein, E. Dietrich, G. Requena, E. Breitbarth, Crack Analysis Tool in Python - Crackpy, 2022.
[61] T. Strohmann, D. Starostin-Penner, E. Breitbarth, G. Requena, Automatic detection of fatigue crack paths using digital image correlation and convolutional neural networks, Fatigue Fract. Eng. Mater. Struct. 44 (2021) 1336–1348.
[62] D. Melching, T. Strohmann, G. Requena, E. Breitbarth, Explainable machine learning for precise fatigue crack tip detection, Sci. Rep. 12 (2022) 9513.
[63] B. Moreno, P. Lopez-Crespo, A.S. Cruces, J. Dominguez, Estimation of the opening load under variable amplitude loading, Fatigue. Fract. Eng. Mater. Struct. 42 (2019) 2194–2203.
[64] Y.C. Yeoh, G. Macchi, E. Jain, B. Gaskey, S. Raman, G. Tay, D. Verdi, A. Patran, A. M. Grande, M. Seita, Multiscale microstructural heterogeneity and mechanical property scatter in Inconel 718 produced by directed energy deposition, J. Alloys Compd. 887 (2021) 161426.
[65] R. Snell, S. Tammas-Williams, L. Chechik, A. Lyle, E. Hernández-Nava, C. Boig, G. Panoutsos, I. Todd, Methods for rapid pore classification in metal additive manufacturing, JOM 72 (2020) 101–109.
[66] T. Shi, J. Li, G. Gao, J. Sun, Z. Yang, J. Yan, G. Qian, Microstructural evolution and formation of fine grains during fatigue crack initiation process of laser powder bed fusion Ni-based superalloy, Addit. Manuf. 85 (2024) 104151.
[67] C. Dayong, L. Wenchang, L. Rongbin, Z. Weihong, Y. Mei, On the accuracy of the X-ray diffraction quantitative phases analysis method in Inconel 718, J. Mater. Sci. 39 (2004) 719–721.
[68] C. Sun, W. Li, C. Li, R. Sun, G. Liu, X. Li, Study on microstructure and fatigue properties of laser powder bed fusion nickel-based superalloy with heat treatment, Additive Manufacturing Frontiers 4 (2025) 200217.
[69] N. Sonntag, B. Piesker, L.A. Ávila Calderón, G. Mohr, B. Rehmer, L. Agudo Jácome, K. Hilgenberg, A. Evans, B. Skrotzki, Tensile and low-cycle fatigue behavior of laser powder bed fused inconel 718 at room and high temperature, Adv. Eng. Mater. 26 (2024).
[70] N.C. Ferreri, S.C. Vogel, M. Knezevic, Determining volume fractions of γ, γ′, γ″, δ, and MC-carbide phases in Inconel 718 as a function of its processing history using an advanced neutron diffraction procedure, Mater. Sci. Eng., A 781 (2020) 139228.
[71] X. Yu, X. Lin, H. Tan, Y. Hu, S. Zhang, F. Liu, H. Yang, W. Huang, Microstructure and fatigue crack growth behavior of Inconel 718 superalloy manufactured by laser directed energy deposition, Int. J. Fatigue. 143 (2021) 106005.
[72] K. Gruber, P. Szymczyk-Ziółkowska, S. Dziuba, S. Duda, P. Zielonka, S. Seitl, G. Lesiuk, Fatigue crack growth characterization of Inconel 718 after additive manufacturing by laser powder bed fusion and heat treatment, Int. J. Fatigue. 166 (2023) 107287.
[73] E. Sadeghi, G. Asala, P. Karimi, D. Deng, J. Moverare, T. Hansson, Fatigue crack initiation and propagation in Alloy 718 with a bimodal grain morphology built via electron beam-powder bed fusion, Mater. Sci. Eng., A 827 (2021) 142051.
[74] C. Pei, D. Shi, H. Yuan, H. Li, Assessment of mechanical properties and fatigue performance of a selective laser melted nickel-base superalloy Inconel 718, Mater. Sci. Eng., A 759 (2019) 278–287.
[75] E. Sadeghi, P. Karimi, R. Esmaeilizadeh, F. Berto, S. Shao, J. Moverare, E. Toyserkani, N. Shamsaei, A state-of-the-art review on fatigue performance of powder bed fusion-built alloy 718, Prog. Mater. Sci. 133 (2023) 101066.
[76] J. Li, Q. Huang, Z. Wang, N. Zhang, G. Chen, G. Qian, Microstructural insights into fatigue short crack propagation resistance and rate fluctuation in a Ni-based superalloy manufactured by laser powder bed fusion, Int. J. Plast. 171 (2023) 103800.
[77] S. Suresh, Fatigue of Materials, second ed., Cambridge University Pess, Cambridge, 1998.
[78] M. Pegritz, S. Wurster, R. Pippan, A. Hohenwarter, Fatigue crack growth of tungsten in the semi-ductile temperature regime, Acta Mater. 317 (2026) 122518.
[79] W. Li, C. Sun, C. Li, G. Liu, Z. Sun, In-situ experimental investigation on fatigue crack growth behavior and crack tip plastic zone evolution of laser powder bed fused TiC/Ti6Al4V composites, Mater. Today Commun. 49 (2025) 113731.
[80] L. Sheridan, O.E. Scott-Emuakpor, T. George, J.E. Gockel, Relating porosity to fatigue failure in additively manufactured alloy 718, Mater. Sci. Eng., A 727 (2018) 170–176.
[81] T.L. Anderson, Fracture Mechanics: Fundamentals and Applications, fourth ed., CRC Press, 2017.
[82] H. Wang, J. Zhang, Y. Li, Z. Wang, J. Wu, Experimental investigation of overload effects on fatigue crack growth behaviour of 7050-T7451 aluminium alloy, Fatig. Fract. Eng. Mater. Struct. 43 (2020) 2928–2942.
[83] H. Tsukuda, H. Ogiyama, T. Shiraishi, Transient fatigue crack growth behaviour following single overloads at high stress ratios, Fatig. Fract. Eng. Mater. Struct. 19 (1996) 879–891.
[84] H. Andersson, C. Persson, In-situ SEM study of fatigue crack growth behaviour in IN718, Int. J. Fatigue. 26 (2004) 211–219.
[85] H.R. Shercliff, N.A. Fleck, Effect of specimen geometry on fatigue crack growth in plane strain—I. Constant amplitude response, Fatigue. Fract. Eng. Mater. Struct. 13 (1990) 287–296.
[86] R. Carlson, G. Kardomateas, P. Bates, The effects of overloads in fatigue crack growth, Int. J. Fatigue. 13 (1991) 453–460.
[87] F. Yusof, P. Lopez-Crespo, P.J. Withers, Effect of overload on crack closure in thick and thin specimens via digital image correlation, Int. J. Fatigue. 56 (2013) 17–24.
[88] G.L.G. Gonzáles, J.A.O. González, J.T.P. Castro, J.L.F. Freire, Detecting fatigue crack closure and crack growth delays after an overload using DIC measurements, in: Fracture, Fatigue, Failure and Damage Evolution 7, River Publishers, New York, 2025, pp. 57–65.
[89] G.L.G. Gonzáles, J.A.O. González, J.L.F. Freire, Characterization of discontinuous crack closure behavior after the application of a single overload cycle, Theor. Appl. Fract. Mech. 114 (2021) 103028.
[90] G. Xin, W. Hangong, K. Xingwu, J. Liangzhou, Analytic solutions to crack tip plastic zone under various loading conditions, Eur. J. Mech. Solid. 29 (2010) 738–745.
[91] R. Hill, A theory of the yielding and plastic flow of anisotropic metals, Proc. R. Soc. Lond. A math, Phys. Sci. 193 (1948) 281–297.
[92] J. Willenborg, R.M. Engle, H.A. Wood, A Crack Growth Retardation Model Using an Effective Stress Concept, 1971.
[93] R.C. McClung, A literature survey on the stability and significance of residual stresses during fatigue, Fatig. Fract. Eng. Mater. Struct. 30 (2007) 173–205.
[94] H.Y. Li, H.L. Sun, P. Bowen, J.F. Knott, Effects of compressive residual stress on short fatigue crack growth in a nickel-based superalloy, Int. J. Fatigue. 108 (2018) 53–61.
[95] D.M. Neto, M.F. Borges, E.R. Sérgio, F.V. Antunes, Effect of residual stresses on fatigue crack growth: a numerical Study based on cumulative plastic strain at the crack tip, Materials 15 (2022) 2156.
[96] O. Karpenko, S. Oterkus, E. Oterkus, Investigating the influence of residual stresses on fatigue crack growth for additively manufactured titanium alloy Ti6Al4V by using peridynamics, Int. J. Fatigue. 155 (2022) 106624.
[97] R. Bao, X. Zhang, Fatigue crack growth behaviour and life prediction for 2324-T39 and 7050-T7451 aluminium alloys under truncated load spectra, Int. J. Fatigue. 32 (2010) 1180–1189.
[98] T. Zhang, R. Bao, S. Lu, B. Fei, Investigation of fatigue crack propagation mechanisms of branching crack in 2324-T39 aluminum alloy thin plates under cyclic loading spectrum, Int. J. Fatigue. 82 (2016) 602–615.
[99] R. VanSickle, D. Foehring, H.B. Chew, J. Lambros, Microstructure effects on fatigue crack growth in additively manufactured Ti–6Al–4V, Mater. Sci. Eng., A 795 (2020) 139993.
[100] W. Li, X. Li, Q. Fang, B. Liu, C. Jiang, Plastically heterogeneity-driven fracture in additive manufactured steels, Eng. Fract. Mech. 283 (2023) 109203.
[101] C. Beachem, Electron Fractography, ASTM International 100 Barr Harbor Drive, PO Box C700, West Conshohocken, PA, 1968, 19428-2959.
[102] Ch Bichler, R. Pippan, Effect of single overloads in ductile metals: a reconsideration, Eng. Fract. Mech. 74 (2007) 1344–1359.
[103] W.J. Mills, C.M. Brown, Fatigue fracture surface morphology for alloy 718, in: Superalloys 718, 625, 706 and Various Derivatives (2001), TMS, 2001, pp. 511–522.
[104] C. Mercer, W.O. Soboyejo, Fatigue crack growth mechanisms in a forged IN 718 nickel-based superalloy, in: Superalloys 718, 625, 706 and Various Derivatives (1997), TMS, 1997, pp. 577–586.